universität wien

MASTERARBEIT

Titel der Masterarbeit

Clash of Porphyroblasts

verfasst von

Hagen Bender, BSc

angestrebter akademischer Grad

Master of Sciences (MSc)

Wien, 2014

Studienkennzahl lt. Studienblatt:	A 066 815
Studienrichtung lt. Studienblatt:	Masterstudium Erdwissenschaften UG2002
Betreuerin / Betreuer:	Univ. Prof. Mag. Dr. Bernhard Grasemann

CLASH OF PORPHYROBLASTS

HAGEN BENDER

Mechanical and chemical interaction of strong objects in a weak deforming matrix and the acceleration of dissolution precipitation creep

Department for Geodynamics and Sedimentology
Faculty of Earth Sciences, Geography and Astronomy
University of Vienna
June 2014

Geologists have a saying –
rocks remember.

— Neil Armstrong

But it is us geologists who learn to read and tell the story petrified within.
In what follows, I present what constituted my last year as a student.

ABSTRACT

The presence of porphyroblasts in metamorphic rocks has a strong influence on the microstructures that develop during deformation. Valuable as gauges for the sense of shear, single isolated porphyroblasts and -clasts have attracted enormous attention and vigorous discussion in the geological community. However, nature does not always provide samples fulfilling this criterion, therefore the understanding of multi-porphyroblast interaction is of great significance.

We use amphibolite-facies garnet mica schists from the Upper Austroalpine Wölz Complex for a case study. The microstructure of mm-cm sized, densely distributed garnet porphyroblasts indicates interference of the blasts. Blasts are subjected to convergence parallel to the instantaneous shortening axis, causing (i) accumulation and deformation of strain caps, (ii) fracturing of the garnets and (iii) dissolution of garnet at collision sites. Parallel to the instantaneous stretching axis, (i) cone-shaped strain shadows are linked between neighbouring garnets and (ii) separation of garnet clusters occurs preferably. Despite the existence of a non-coaxial strain component, strain shadows do not develop a monoclinic symmetry, owing to the interference of adjacent blasts.

The major part of deformation is accommodated by dissolution precipitation creep. Using multiple methods for quantifying the strain, this study demonstrates the effectiveness of dissolution precipitation as deformation mechanism for high-grade metapelites.

Quantitative chemical analysis and thermodynamic modelling are utilised to examine compositional variations in minerals. The results show that in these fluid-saturated rocks no deviations from lithostatic pressure are recorded by the present-day assemblage.

ZUSAMMENFASSUNG

Porphyroblasten haben einen starken Einfluss auf das bei Deformation entstehende Mikrogefüge. Einzelne, isolierte Porphyroblasten und -klasten sind wertvolle Hilfsmittel bei der Bestimmung des Schersinns in Scherzonen. Daher wurde ihnen nicht nur eine enorme Aufmerksamkeit in der geologischen Gemeinde zuteil, sie wurden auch angeregt diskutiert. Die Natur jedoch, bietet nicht immer ideale Bedingungen zur Analyse von isolierten Porphyroblasten, daher ist das Verständnis der Interaktion in Populationen von Porphyroblasten von großer Bedeutung. Wir untersuchen amphibolitfazielle Granatglimmerschiefer aus dem Wölz Komplex des Oberen Ostalpins als Fallbeispiel. Das Mikrogefüge von mm-cm großen, dicht verteilten Granatporphyroblasten zeigt an, dass die Blasten miteinander interagieren. Porphyroblasten nähern sich parallel zur momentanen Verkürzungsrichtung aneinander an und verursachen: (i) Verdichtung und Akkumulierung von strain caps, (ii) Zerbrechen der Granate und (iii) Drucklösung von Granat in

Kollisionszonen. Parallel zur momentanen Streckungsrichtung (i) verbinden sich kegelförmige strain shadows zwischen benachbarten Granaten und (ii) trennen sich Granat-Polykristall-Cluster bevorzugt. Durch die Interaktion der Granate bilden sich keine monoklinen Gefüge aus, obwohl es eine nicht-koaxiale Deformationskomponente gibt.

Der Hauptteil der Deformation wird durch Drucklösungskriechen (dissolution precipitation creep) aufgenommen. Mehrere Methoden der Strainquantifizierung werden angewandt. Damit kann gezeigt werden, dass Drücklösungskriechen ein äußerst effektiver Deformationsmechanismus für hochgradig metamorphe Metapelite ist.

Mittels quantitativer chemischer Analyse und unter Verwendung von thermodynamischer Modellierung werden Variationen in der Mineralzusammensetzung untersucht. Die Ergebnisse zeigen, dass die heutige Mineralparagenese für diese Art von fluid-gesättigten Gesteinen keine Abweichungen vom lithostatischen Druck aufzeichnet.

ACKNOWLEDGMENTS

First and foremost I want to thank my advisors Benjamin Huet and Bernhard Grasemann for their support and guidance throughout the whole research for my Master's project. Particularly I would like to thank Benjamin Huet most sincerely for the uncountable hours we spent discussing, calculating and scripting. Their assistance and help encouraged me to achieve this final state of my thesis.

Ralf Schuster is greatly thanked for his lead in the field and vivid discussions about the regional impact of this study. I also want to thank Ralf Schuster and the laboratory staff at the Geological Survey of Austria for the extremely fast processing whole rock analyses. Many thanks to Hugh Rice whose support in the field and frequent advice is gratefully acknowledged. I am obliged to the whole Structural Processes Group for the pleasant surrounding during my final year, especially Martin Schöpfer, Norbert Kohlmayer, Anna Rogowitz, Maarten Voorn, Marco Lommatzsch and Tom Griffiths for discussions and their helpfulness to solve geological problems. Many thanks to Andreas Gerner for supporting me with LaTeX issues.

I thank Franz Kiraly and Theodoros Ntaflos for their assistance at the electron microprobe. Claudia Beybel, Leopold Slawek and Sigrid Hrabe are thanked for their exceptional preparation of thin sections.

The pleasant companionship in both semesters I felt 'home', the freshmen from 2008 and 2009, enriched my studies a lot. I thank my fellow students for joint learnig sessions and philosophising in the field as well as for the fun and drinks we shared on excursions. Thanks to Arthur Grebenicek, Chloé Asmar, Christian Steinbauer, Christopher Kollmann, David Heuser, Elijah Dippenaar, Franziska Mayrhofer, Georg Hatzenbichler, Harald Bauer, Ivanka Mitrovic, Johannes Loisl, Jürgen Österle, Karoline Lindner, Katharina Böhm, Leonhard Brunauer, Mathias Bichler, Martin Walter, Martina Lan Salomon and Wolfgang Knierzinger.

Last and most importantly, thank you, Anna, for supporting me throughout all the years of my studies. For keeping me motivated, for encouraging me to think outside the box (made of rocks), for being understanding for all the long hours I spent in university and for the all the good times we shared in the last five years!

CONTENTS

LIST OF FIGURES

LIST OF TABLES

ACRONYMS

BSE Backscattered electron

CD Cleavage domain

DTNNM delaunay nearest neighbour triangulation method

DPC Dissolution precipitaion creep

EMP Electron microprobe

MZ Microfold hinge zone

SS Strain shadow

SC Strain cap

Zone-(i)-fabrics Internal microstructural domain within garnet, characterised by planar orientation of inclusions

Zone-(ii)-fabrics More external microstructural domain within garnet, characterised by folded and crenulated inclusion trails

Part I

INTRODUCTION

1 INTRODUCTION

Porphyroblastic minerals provide insight into a broad variety of geological processes that are only preserved due to their occurrence. Implications that can be drawn from studying porphyroblasts are far too versatile to depict them here entirely. Notable information that porphyroblasts can provide, shed light on the deformational and metamorphic history of a rock. Some selective aspects that are recorded by porphyroblasts include the following. Internal inclusion fabrics mimic older microstructures that are interpreted as relicts of earlier stages of deformation or the undeformed protolith (e.g. Stöckhert et al., 1997; Johnson, 1999; Passchier and Trouw, 2005). Composition and variations in composition in porphyroblasts are dependant on the PT conditions during growth or are subjected to chemical alteration (e.g. Gaidies et al., 2006; Bestel et al., 2009; Caddick and Kohn, 2013; Ague and Carlson, 2013; Baxter et al., 2013, and references therein). Probably most eminent, at least in structural geology, is the ability of porphyroblasts and -clats to record the sense of shear. Consequently, they constitute valuable tools for shear zone analysis (e.g. Passchier and Simpson, 1986; Mancktelow, 2013; Marques et al., 2014, for a recent review of inclusions in viscous flow). The main emphasis has been laid on the understanding of single, isolated inclusions in a deforming matrix. Both setups, a strong inclusion in a less viscous matrix and vice versa have been subject of analytical and numerical simulations as well as laboratory and field studies (e.g. Schmid and Podladchikov, 2003; Marques et al., 2014). However, naturally, strong inclusions often occur in populations, which causes complex interaction of the inclusions among themselves and with their matrix. Interference can lead to counterintuitive strain patterns that are wrongly interpreted when interpolating the knowledge gained from the study of single objects (Ildefonse et al., 1992). The different mechanical and rheological behaviour two- or multiple-phase compounds affect far more geological phenomena than porphyroblast or -clast populations in strained rocks. Because of this diversity, associated problems and questions have been addressed interdisciplinary within the Earth Sciences. Crystals distributed in a melt, pegmatites where quartz is scattered in a feldspathic (stronger) matrix or sediment dispersions in water, ice or air are just some instances that reflect the importance of understanding inclusion-matrix systems (e.g. Dell'Angelo and Tullis, 1996; Piazolo et al., 2002; Groome et al., 2006; Jessell et al., 2009; Johnson et al., 2009; Deubelbeiss et al., 2011). In the last two decades the efforts to investigate such systems has risen constantly. While analogue modelling could successfully show how geometries, for instance shape preferred orientations, develop in populations of elongated objects (Arbaret et al., 1996), the insights extended to implications on the vorticity and rheology (Piazolo et al., 2002). More recently, numerical models were used to obtain constraints on the flow kinematics and rheology of magma (Deubelbeiss et al., 2011; Yamato et al., 2012). The

cognition that the presence and interaction of strong inclusions in a ductile Newtonian fluid causes a non-Newtonian bulk rheology is particularly interesting. Deubelbeiss et al. (2011) show that, in viscous flow, interacting strong inclusions accumulate parallel to the instantaneous shortening direction, forming so called 'force chains'. These in turn, cause high differential stresses in the interior of the grains which can possibly trigger fracturing. Despite the opportunities of measuring physical quantities directly, models cannot fully resemble the complexity of geological processes. Therefore, models may not always be able to emulate or predict natural observations (Pennacchioni et al., 2001). This study investigates how porphyroblast interaction is preserved in a garnet mica schist from the Upper Austroalpine Wölz Unit. The samples are rocks from a well studied area which is part of the Eoalpine extruding wedge (Schuster et al., 2004; Schmid et al., 2004; Gaidies et al., 2006; Bestel et al., 2009). This study gives a classification of microstructures that are caused by interfering blasts in the particular samples. Secondly, variations in local pressure and the possibility to preserve them in rocks is discussed in the face of results of quantitative chemical analysis and thermodynamic modelling. Eventually, the bulk strain for the studied samples that is accommodated by dissolution precipitation creep is estimated which demonstrates the significance of dissolution precipitation in high-grade metapelitic rocks.

2 GEODYNAMIC SETTING

The Wölz Complex is part of the Koralple-Wölz nappe system of the Eastern Alps. The latter constitute the eastern portion of the Alpine mountain belt that was build by two distinct orogenic cycles during the convergence of Europe and the Apulian plate (Froitzheim et al., 1996; Schmid et al., 2004). The first event is the Cretaceous Eoalpine continental collision that followed the subduction of Meliata, an embayment of the Tethys ocean (Thöni and Jagoutz, 1993). A second orogenic event, referred to as the the Tertiary Alpine event, is related to the S-directed subduction of the Penninic ocean below Apulia (Frisch et al., 1993).

During the Eoalpine event, the northern realm of the Apulia microcontinent was subjected to essential E-W directed shortening due to intracontinental subduction. This lead to the formation of thrust sheets in upper crustal levels whereas lower crustal parts were subducted below more southern parts of Apulia, acting as the tectonic lower plate. These units north of the subduction zone are referred to as the Austroalpine nappes (Schmid et al., 2004). The units that were part of the subduction channel experienced pressure-dominated metamorphism. Within the Austroalpine nappe stack, the metamorphic grade increases from the structurally lowest nappes towards the Koralpe-Wölz nappe system and decreases again towards the structurally highest nappes (Schuster et al., 2004). The central part of the Koralpe-Wölz nappe system, the Saualpe-Koralpe Complex contains the Eoalpine eclogites (Thöni and Jagoutz, 1993). A gradual decease in metamorphic condition towards amphibolite to greenschist facies conditions is observed towards the structurally lower Wölz Complex. The latter is mainly constituted by metapelites with intercalations of amphibolites that record a polymetamorphic history (Faryad and Hoinkes, 2003; Gaidies et al., 2008; Bestel et al., 2009). Garnet mica schists are typical lithologies. In places, garnet is characterised by two marked growth zones (Schuster and Thöni, 1996). The inner garnet zone represents Permian LP/HT metamorphism ($\sim 0.4 \pm 0.05$ GPa and 535 ± 20°C at the onset of garnet growth, Gaidies et al., 2008) that was dated 269 ± 4 Ma (Schuster and Thöni, 1996). A second zone of garnet overgrew these Permian cores (Habler and Thöni, 2001). The second type of garnet is associated with Eoalpine HP/HT metamorphism ($\sim 0.65 \pm 0.05$ GPa and 540 ± 10°C at the onset of garnet growth, Gaidies et al., 2008) and is dated at 94 ± 15 Ma (Schuster and Thöni, 1996). The Permian garnet is, however, not present everywhere. Where absent, Eoalpine garnet occurs alone. The here studied garnets in mica schists from the Steinplan area are such single-phase Eoalpine garnets.

3

METHODS

Throughout this study the labelling of samples and images is coded like *01a1_001*, where *01* is the number of the sample and location of sampling, *a* is the label of the slice cut from this sample, *1* is the number of the thin section prepared from the rock plate and *_001* refers to the number and location within the thin section when many images were taken. Italic font is chosen here for better legibility. In the following, regular font will be used.

Thin sections were prepared from selected samples in the XZ plane (X>Y>Z axes of the finite strain ellipse), i.e. perpendicular to the foliation and parallel to the mineral stretching lineation. For a table including sampling locations and brief descriptions see Appendix v. Sets of common $\sim 40 \times 20$ mm sized thin sections were produced at a thickness of 30 µm as well as 80 µm, respectively. Additionally, large $\sim 1250 \times 85$ mm thin sections were manufactured at a thickness of ca. 200 µm. Microstructural analysis was carried out using optical and electron microscopy. Backscattered electron image acquisition was done with a FEI Inspect S50 SEM at the Department of Lithospheric Research, University of Vienna. The images were taken at 15kV acceleration voltage. The equipped X-ray-dispersive detector EDAX Apollo XV was utilised to qualitatively characterise phases and to collect qualitative element distribution maps. Quantitative chemical analysis was done using the CAMECA SX100 electron probe micro analyser at the Department of Lithospheric Research, University of Vienna. The EMP was operated at 20 kV acceleration voltage, 15 nA beam current and a spot size of 1 µm. Defocusing to 5 µm was applied for phyllosilicates and feldspar analyses. The calibration for the respective elements was done with following minerals: Si - quartz, Al - almandine, Ti - rutile, Mg - olivine, Fe - almandine, Mn - spessartine, Zn - gahnite, Ca - wollastonite, Na - albite and K - orthoclase. Mineral formula calculation was done using MINSORT (Petrakakis and Dietrich, 1985).

Images of thin sections were captured as described in the following. Small thin sections were either scanned using the Nikon COOLSCAN V ED Filmscanner or photographed from an optical microscope. Large thin sections were either scanned using a flatbed scanner or photographed in transmitted light using a digital camera. Images of the thin sections were digitised redrawing the outlines of the minerals or microstructural domains in Adobe Illustrator CS3 and CS4. Finally, 8-bit grey scale raster graphics were generated. For further processing the ImageJ-based (Rasband, 1997) open-source program Fiji (Schindelin et al., 2012) was used.

Part II

PETROSTRUCTURAL ANALYSIS

4 MICROSTRUCTURAL ANALYSIS

4.1 OUTCROP DESCRIPTION

The studied outcrops lie along a forest road near the peak of the mountain Steinplan in Southwest Styria, Austria (UTM33T, 492800E, 5223250N, Fig. 1). Garnet-kyanite-staurolite mica schists of the Wölz Complex are the major lithology throughout the working area. A foliation-parallel layer of garnet amphibolite of ~10 m thickness is located in the eastern part of the study area. The contact to the structurally lower biotite amphibolites of the Speick Complex strikes around the peak of Steinplan. A detailed description of the outcrops of the porphyroblast-rich mica schists is done in the following.

Most distinctive is the main foliation s_m which dips intermediately towards the S to SW. The mineral stretching lineation l_m plunges shallowly towards the S (Fig. 3a). It is associated with a top-to-the-N sense of shear, constrained by σ-type strain shadows around isolated garnet crystals. The main foliation originates from an earlier crenulation cleavage s_{cr1} (Figs. 2b, c). Associated hinges l_{cr1} are sub-parallel to l_m. A second crenulation developed during a later, lower-grade stage of deformation, resulting in widely spaced microfolds of s_m. The hinges of these folds strike E-W, perpendicular to l_m and l_{cr1} (Figs. 2d, 3a, b). The fabric is strongly influenced by densely distributed porphyroblasts of garnet, kyanite and staurolite. Garnet is the most abundant porphyroblastic mineral ($15-20$ % mode). Therefore and for simplicity, the rocks will be referred to as garnet mica schists in the following. A variation in size of garnet grains can be observed throughout the study area. Garnets are typically $1-3$ cm in diameter. The samples collected at the sites 10 and 11 are, however, exceptional. There, garnet grains measure ~3 mm across. Kyanite ($1-5$ % mode) crystals show a shape preferred orientation. Their long axes are aligned parallel to the X-axis of finite strain. Staurolite (~1 % mode) occurrence is highly variable throughout the study area. In sample 08, the mode reaches ~12 %. Yet, commonly staurolite constitutes the least frequent porphyroblasts. Due to the interference between porphyroblasts and matrix the strain pattern is very heterogeneous (Figs. 2, 3). Microstructural investigation was conducted on the samples 03, 07, 08, 10 and 15 which helped to decipher and understand the complex fabric.

4.2 MICROSTRUCTURAL DESCRIPTION

The mineral assemblage contains almandine-rich garnet, phengite, paragonite, quartz, kyanite, staurolite, biotite, epidote, plagioclase and accessory apatite, rutile, ilmenite, tourmaline and graphite. Additionally, chloritoid and pyrite are preserved as inclusions in garnet. Chlorite exists as a retrograde feature. Owing to the presence of graphite, the samples are darkly coloured. The microstruc-

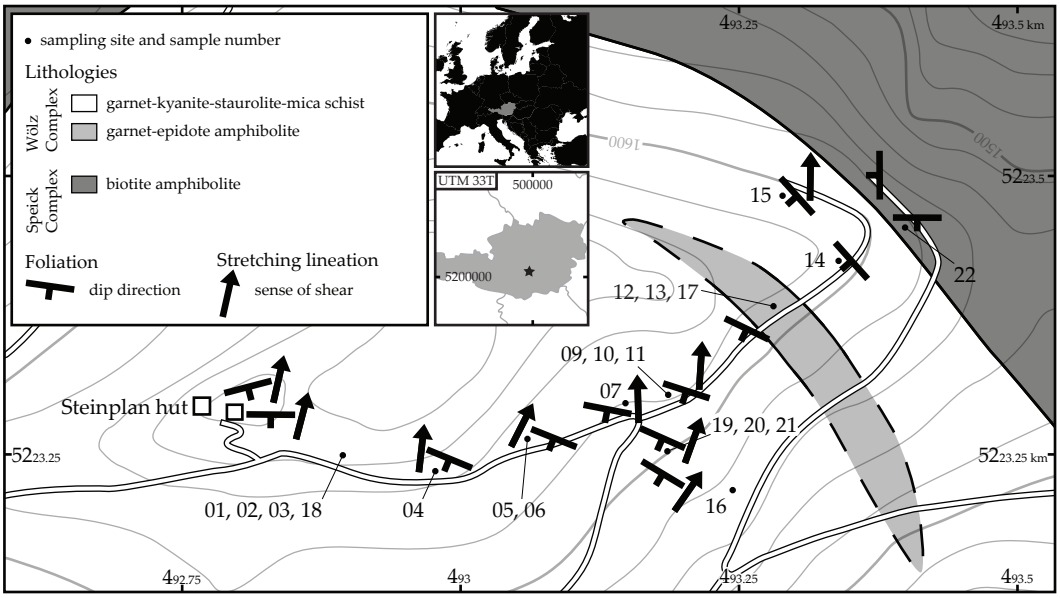

Figure 1: Geological and structural map of the Steinplan area. UTM coordinates.

ture can be literally described as a response to the abundance of densely populated porphyroblasts. The foliation wraps around the blasts which are adjacent to strain caps and strain shadows. Moreover, the strain shadows and foliated realms appear well segregated, suggesting that dissolution precipitation creep (DPC) was active. Dissolution precipitation creep is driven by gradients in chemical potential that develop due to local differences in pressure (Gratier et al., 2013; Wassmann and Stöckhert, 2013b). Mass transfer is occurring from sites of higher differential stress, such as loaded phase boundaries, towards sites of lower differential stress, such as sites of dilation. The full process of dissolution precipitation creep includes the sequence of dissolution, transport via diffusion through a fluid phase and is followed by precipitation (Gratier et al., 2013). Because the distinction of dissolution sites and precipitation sites is relatively simple in the samples, it is feasible to categorise the microstructure based on the juxtaposition of sources and sinks for mobile phases. Four different microstructural domains are defined: (i) Cleavage domain (CD) and (ii) Strain cap (SC) as sites of dissolution and (iii) Microfold hinge zone (MZ) and (iv) Strain shadow (SS) as sites of precipitation. These categories resemble end members of the observed fabrics. The classification is based on the mechanism of their development rather than their geometrical peculiarity, plainly because the microfabric is so diverse. In the following, I characterise the aforementioned microstructural domains which I used to classify typical microstructures.

CLEAVAGE DOMAINS (CD) Intercalated phengite and paragonite, in equal amounts, establish the main foliation in the CD domains. CD domains are depleted in quartz. The aforementioned accessory minerals are typically aligned parallel to the finite stretching direction if they are elongated. Graphite causes a dark colour. The cleavage domains show the characteristics of a crenulation cleavage (Passchier and Trouw, 2005).

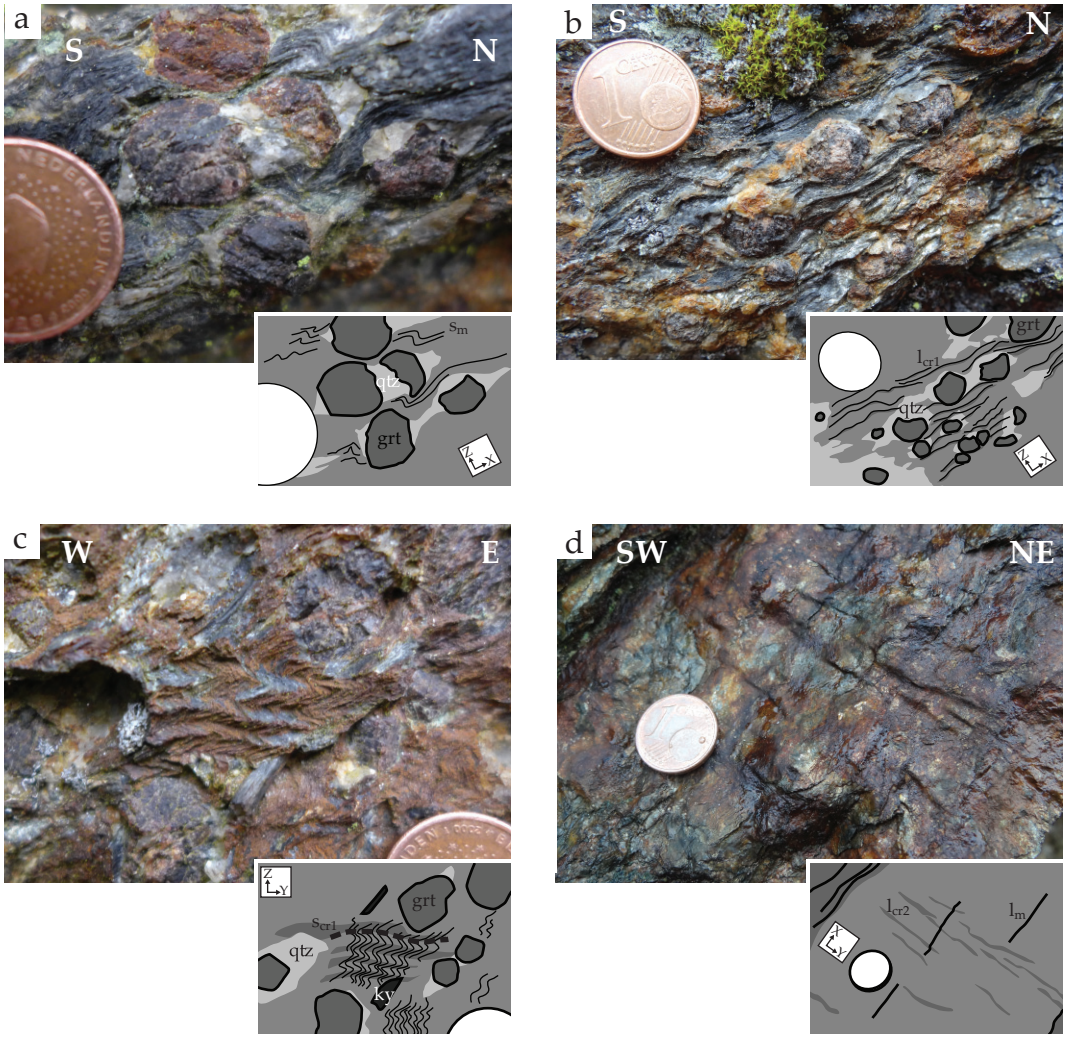

Figure 2: (a-d) Field photos of the studied garnet mica schists. UTM coordinates, zone 33T: a-c: 5223269N, 493257E (sampling sites 19-20, see Fig. 1); d: 5223316N, 493248E. (a) Interacting garnet crystals with linked strain shadows in X-direction. Note the uppermost garnet impinging the gap in between the garnets below. (b) Note that the main foliation is only marked by the crests of *cr*1 crenulation. (c) Almost chevron-type folding of an older foliation. The iron-stained fold limbs indicate s_{cr1} respectively s_m (which are parallel). (d) Foliation plane with *cr*2 folds.

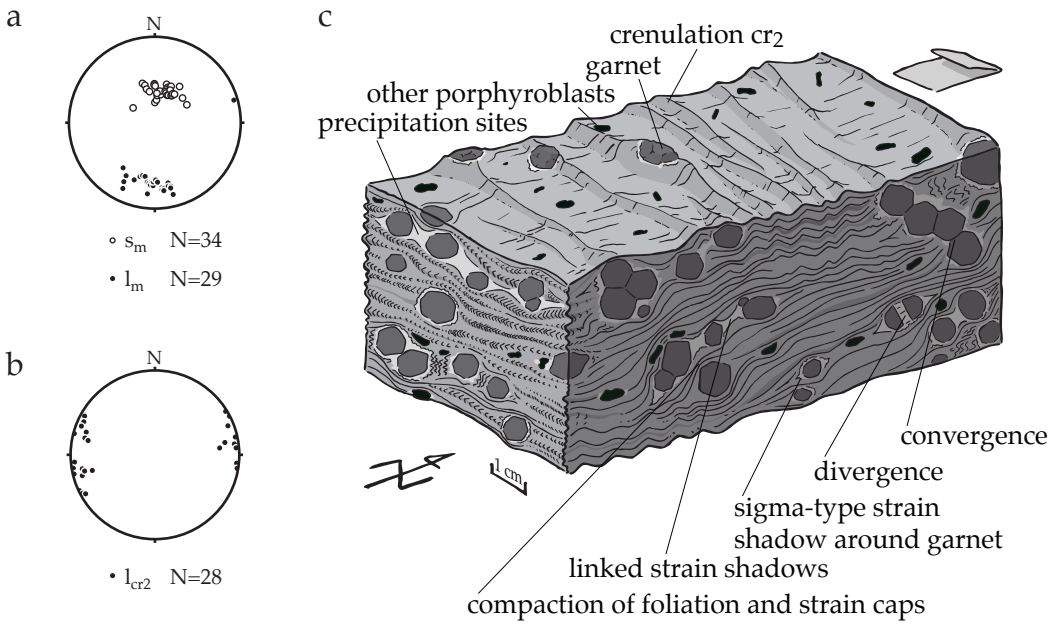

Figure 3: (a) Lower hemisphere equal-area plot of main foliation s_m and mineral stretching lineation lm. (b) Lower hemisphere equal-area plot of l_{cr2} hinges. (c) Synoptical diagram (not to scale) summarising field observations.

STRAIN CAPS (SC) Strain caps are domains of condensed foliation that develop around strong inclusions in the quadrants of instantaneous shortening. Typically they are enriched in less soluble phases which are passively enriched after the removal of mobile phases (Passchier and Trouw, 2005). According to this general definition of strain caps, strain is enhanced in these regions as compared to the matrix. In the studied samples, SC domains comprise cleavage domains in the direct vicinity of porphyroblasts and are strongly foliated. SC domains are even subjected to a further increase in strain due the convergence of garnets, as a consequence of porphyroblast interaction. Associated phenomena are described below in further detail.

MICROFOLD HINGE ZONES (MZ) MZ domains are essentially saddle reef structures which develop in the dilational regimes of fold hinges (Ramsay, 1974). Folding of white mica in crenulation domains of $cr1$ results in the development of precipitation sites (mostly saddle reef structures, Fig. 4d) which are preserved in microlithons. For this reason microlithons are counted as MZ domain as well, even though they are no sites of continuous precipitation, i.e. MZ are not fully reprecipitated. I do so in order to juxtapose these domains of matrix where precipitation occurs locally, in opposition to CD domains of matrix, which are places of dissolution. Mineralogically, these domains consist mainly of white mica, quartz, biotite and are poor in graphite. The general appearance of these domains is characterised by obliquely oriented mica grains in respect to the cleavage domains. A crenulation of an older foliation is well preserved and, in places, is traced by en-echelon oriented rutile grains that trace the microfolds.

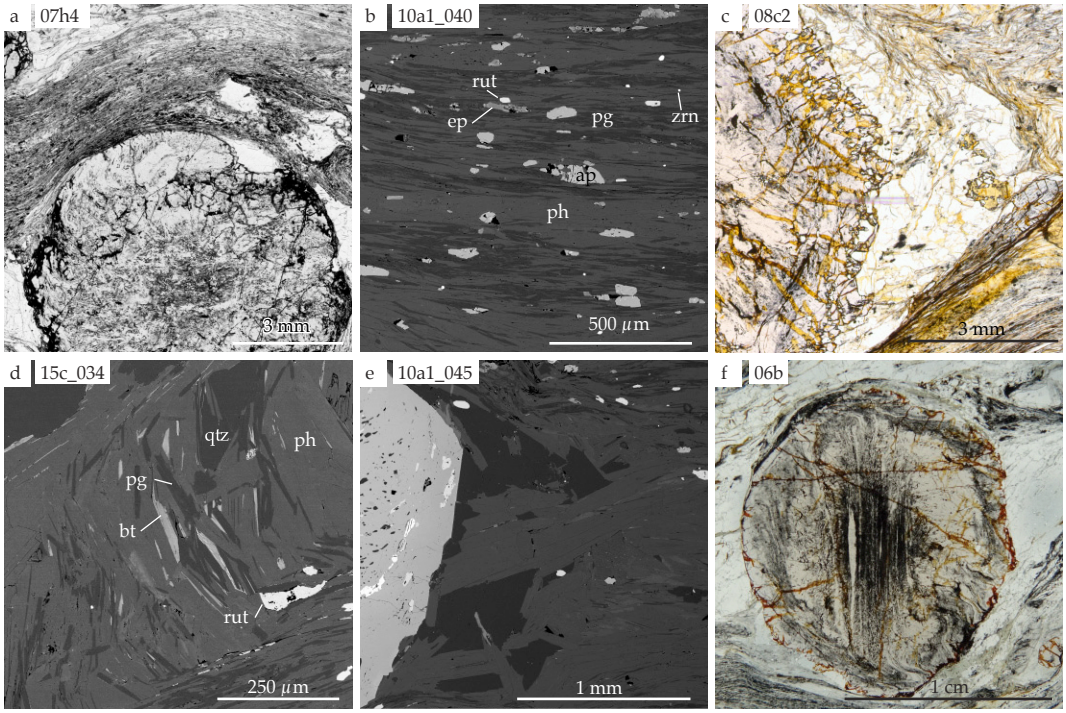

Figure 4: Compilation of observed microstructures. Image labels in upper left corners. Mineral abbreviations: qtz - quartz, ph - phengite, pg - paragonite, bt - biotite, rut - rutile, ep - epidote, ap - apatite, zrn - zircon. (a) Scanned thin section showing an undisturbed strain cap. (b) BSE image of foliated matrix. Typical appearance of CD domains. (c) Scanned thin section of an undisturbed, cone-shaped strain shadow. (d) BSE image of a crenulated microlithon. Typical appearance of microfold hinge zones, i.e. MZ domains. Note the site of biotite resemble saddle reef structures. (e) BSE image of a strain shadow, i.e. typical SS domain. (f) Photograph of a large thin section. Zone-(i)-fabrics are well developed in the interior of the garnet. The rim of this garnet (rich in opaque inclusions) depicts a transition to Zone-(ii)-fabrics. The zones (i) and (ii) are defined in the paragraph 4.2.

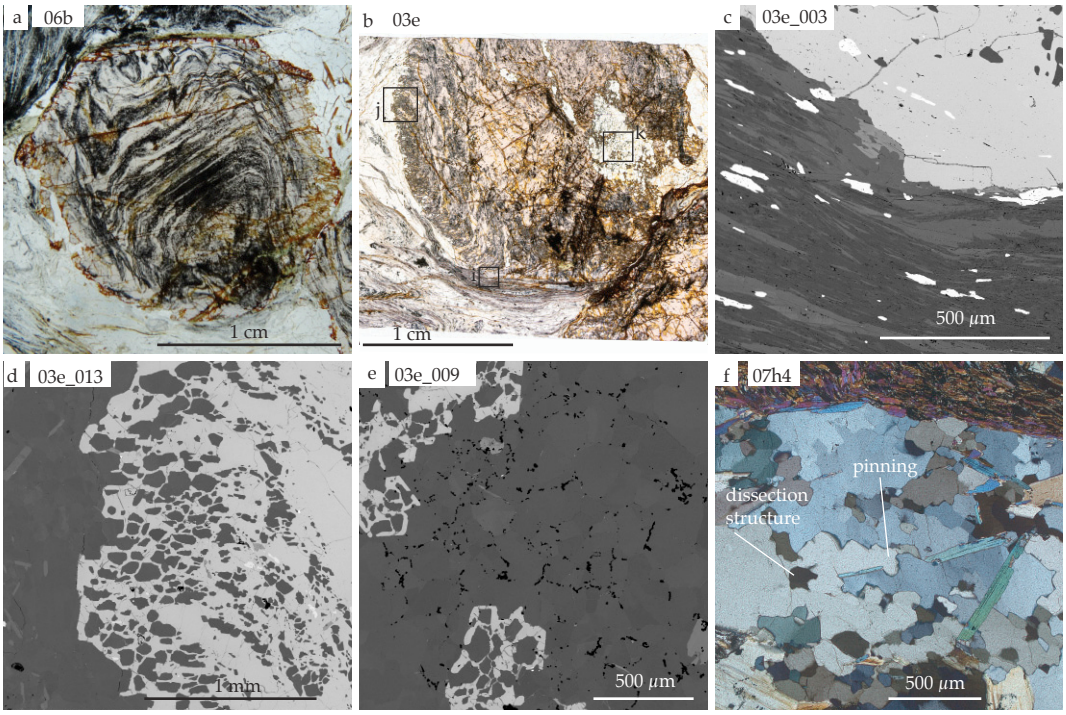

Figure 5: Compilation of observed microstructures. Image labels in upper left corners. (a) Photograph of a large thin section showing the complete succession of observed internal fabrics in garnet from core to rim: (i) planar Zone-(i)-fabrics, (ii) folded Zone-(ii)-fabrics and a graphite poor rim in the upper left part of the grain. (b) Scanned thin section of poikiloblastic garnet. Squares indicate the location of sub-figures i-k. (c) BSE image showing overgrowth of a strain cap by garnet. (d) BSE image of garnet overgrowth of a strain shadow. (e) BSE image displaying foam-structured quartz inside garnet. Net-like honeycomb garnet (Hawkins et al., 2007) delineates former quartz grain boundaries in the upper left and lower middle part of the image. In places, garnet does not fully encompass quartz grains yet. Note the graphite tracing grain boundaries of quartz indicating static recrystallisation of quartz (Drury and Urai, 1990). (f) Optical micrograph (crossed polarisers, compensator red I inserted) a SS domain. Note the features typical of grain boundary migration dynamic recrystallisation: lobate grain boundaries, large grain size (up to almost 1 mm in this image), pinning and dissection structures (Stipp et al., 2002).

STRAIN SHADOWS (SS) Strain shadows are constituted of minerals that precipitated adjacent to strong inclusions in the quadrants of instantaneous stretching. Usually they are characterised by an unoriented fabric of equidimensional grains (Passchier and Trouw, 2005, Figs. 4c, e). SS domains comprise mainly quartz and white mica. Phengite and paragonite are, however, not equally distributed like in the CD and SC domains. Phengite is far more abundant than paragonite at a ratio of ca. 9 : 1 (Fig. 4e). Further precipitated minerals include biotite and kyanite. The occurrence of biotite solely in precipitation sites is striking. Quartz displays dynamic recrystallisation with characteristics typical of grain boundary migration (Stipp et al., 2002). Grain boundaries show interfingering and lobate shapes. Pinning and dissection structures are commonly observed (Fig. 5f). Quartz grains are large in size (up to 1 mm) where no other phases limit grain growth (Fig. 5f). If other phases, e.g. white mica, are present the size is limited to the intermediate space. Undulose extinction is distinct. Because graphite is absent, SS domains are easily distinguishable. Like the other microstructural domains, the here defined SS domains are not only strain shadows per se, but assignments to the classification SS for sites which resemble strain shadows but are not in direct vicinity of porphyroblasts.

GARNET Garnet grains are sub-euhedral and sometimes form polycrystal clusters. Usually polycrystals are composed of < 5 nuclei. Individual crystals are difficult to detect in the optical microscope. Concave grain boundaries and inclusion trails which transect garnet clusters at suspected grain boundaries often indicate polycrystals. This, however, renders a somewhat arbitrary way of identifying individual grains in a cluster. Element distribution maps of Mn depict different nuclei of a polycrystal unambiguously (Fig. 8d). Nevertheless, polycrystals do not always show distinct growth zoning patterns for each crystal (Whitney and Seaton, 2010). In other words, growth zoning patterns of individual grains cannot be expected in a polycrystal. Vice versa, concentric zoning patterns around different nuclei give evidence for clustered nucleation or impingement of multiple grains during growth (Spiess et al., 2001; Whitney and Seaton, 2010). Mineral inclusions of quartz, white mica, chloritoid, apatite, rutile, epidote, K-feldspar, pyrite and graphite preserve an older fabric. Chloritoid and pyrite occur exclusively as inclusions in garnet and do not appear in the matrix. The internal fabric shows microstructural zoning of (i) an internal realm that is characterised by a rather straight to slightly curved alignment of inclusion phases. These planar features show no coherent orientation among themselves and do not find continuity with the external fabric in the matrix. In an outer zone (ii), the older foliation is crenulated or bent. In some cases, Zone-(i)-fabrics gradually blend to Zone-(ii)-fabrics which result in sigmoidal and millipede structures (Fig. 5a), the origin of which is highly debated (Johnson and Bell, 1996). This transition is, however, not visible in every grain. In some cases garnets exhibit a thin rim that is marked by a sharp decrease in graphite content. Large garnet grains often record the overgrowth of strain caps and strain shadows in the respective quadrants of the instantaneous stretching axes.

Some of the centimetre-sized garnets preserve a net-like structure of thin garnets walls in between foam-structured quartz grains which has been previously described as honeycomb garnet (Figs. 5b, e; Stöckhert et al., 1997; Hawkins et al., 2007). The grain boundaries of foam-structured garnet are, however, not everywhere traced by garnet. Where garnet is absent, quartz-quartz boundaries are delineated by graphite (Fig. 5e). The quartz crystals lack undulose extinction in these domains. Quartz grains are equidimensional and several tens of micrometers in size.

Additionally to the afore described internal fabrics, some garnets show textural sector-zoning. Associated microfabrics are Type-I inclusion trails that consist of incorporated matrix minerals, Type-II-intergrowths which are tubular quartz inclusions that grew simultaneously with garnet. Another feature typical of textural sector-zoning are cleavage domes which are also observed. Cleavage domes are crystal-face-parallel accumulations of less soluble matrix components, in this case graphite (Rice and Mitchell, 1991; Rice et al., 2006, and references therein; Fig. 4f, 5b, 7c).

OTHER PORPHYROBLASTS Beside to garnet, kyanite and staurolite appear as porphyroblastic minerals. They preserve similar internal fabrics as garnet crystals. These fabrics, however, do not show systematic patterns as described for garnet. Yet, kyanite and staurolite preserve an older fabric as well, similar to Zone-(i)-fabrics in garnet. Overgrowth relationships between staurolite and garnet indicate that garnet grew prior to staurolite.

4.3 INTERACTION OF PORPHYROBLASTS

The deformation of the host rock results in relative movement among porphyroblasts. This in turn causes various phenomena of porphyroblast-porphyroblast as well as porphyroblast-matrix interferences. The analysis of porphyroblast-porphyroblast interactions was done on the basis of garnet-garnet interactions because the latter is the most abundant porphyroblastic mineral. Four scenarios of movement of garnets relative to each other are possible: convergence (i) parallel to the instantaneous shortening axis and (ii) in the field of incremental shortening as well as divergence (iii) parallel to the instantaneous stretching axis and (iv) in the field of incremental lengthening. Because the microstructural record indicates that co-axial deformation was prevailing, the Z axis of finite strain and the instantaneous shortening axis as well as the X axis of finite strain and the instantaneous stretching axis coincide. This accordance is, however, just approximate because the deformation is strongly dependant on the local abundance of porphyroblasts. Nevertheless it can be inferred that the plane of the thin section (XZ) is the correct plane to observe convergence and divergence of garnets.

CONVERGENCE Approaching garnets cause deformation in the intermediate matrix which is constricted in between the blasts. Foliation planes thus show narrower spacing than in undisturbed strain caps. Upon continuous convergence these domains are subjected to increased dissolution until the soluble phases

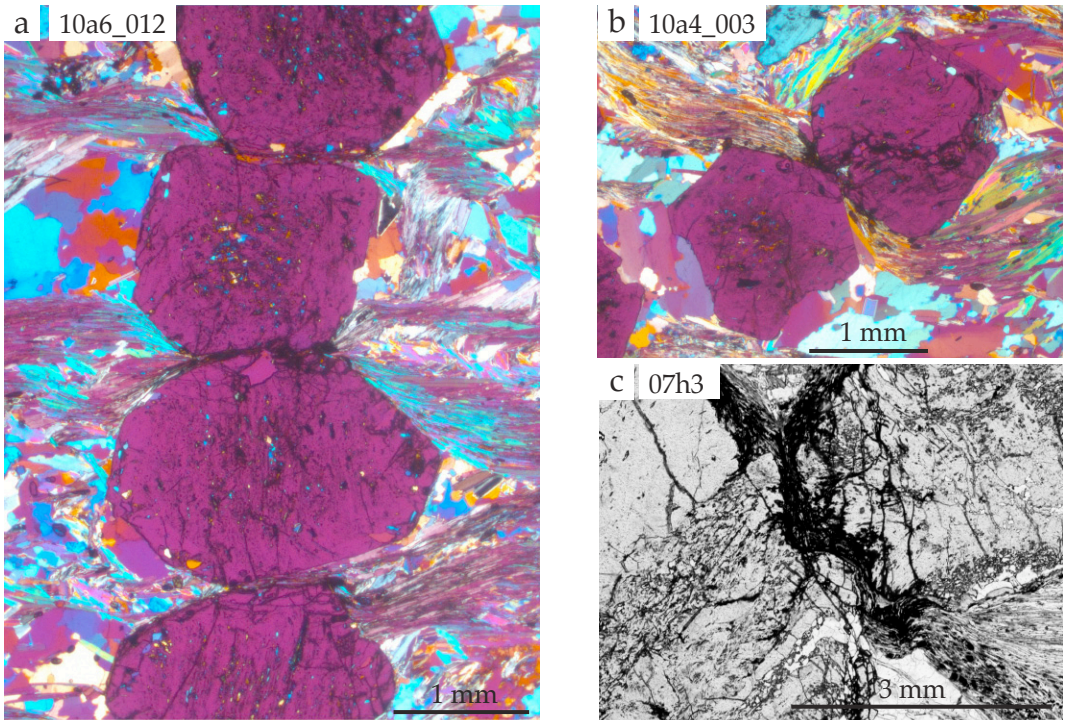

Figure 6: Microstructures that developed as a consequence of garnet convergence. Image labels in upper left corners. (a) Optical micrograph (crossed polarisers and compensator red I inserted) of four in-series garnets that collided. Note that the intermediate matrix has been dissolved almost completely. The uppermost garnet slightly indents the grain below. (b) Optical micrograph (crossed polarisers and compensator red I inserted) showing oblique convergence of garnets resulting in depletion of the matrix. (c) Scanned thin section exhibiting stylolitic garnet dissolution. Note the graphite rich dissolution seam.

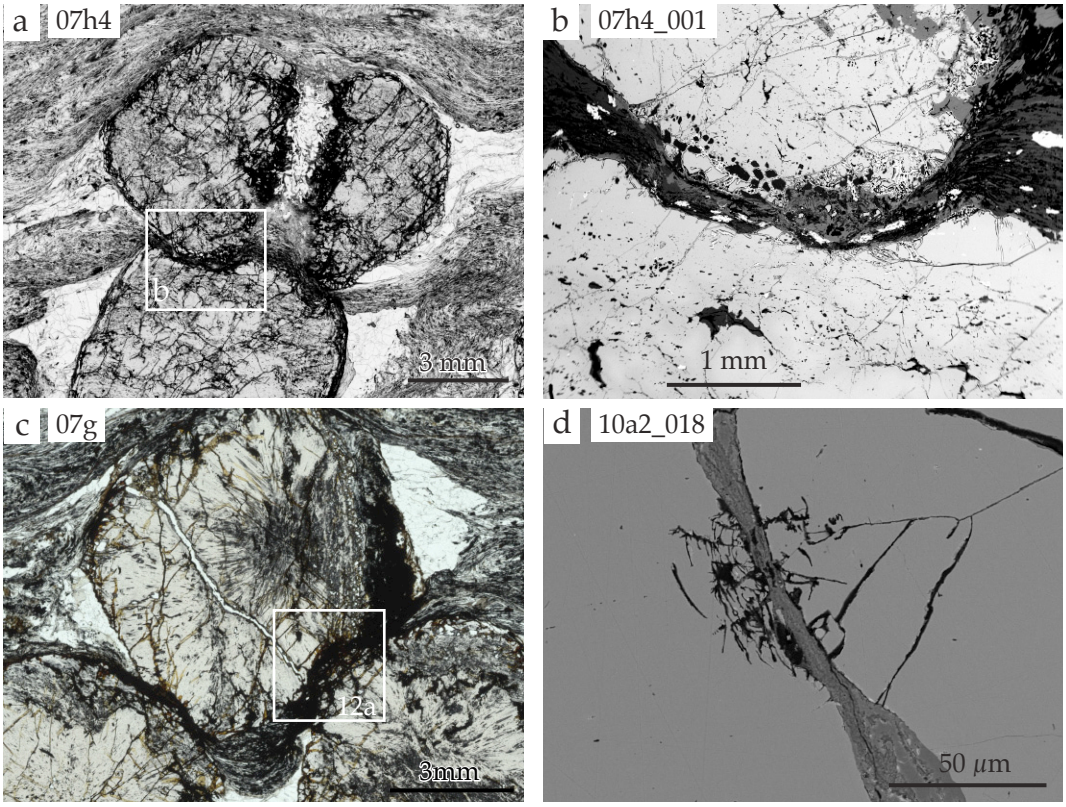

Figure 7: Microstructures that developed as a consequence of garnet convergence. Image labels in upper left corners. (a) Scanned thin section of coincidental dissolution of the lower garnet by two fragments of a former polycrystal which was separated due to collision. (b) BSE image of a dissolution seam that is enriched in rutile (bright grains). (c) Scanned thin section showing the indentation by dissolution of the upper garnet by the lower right one. The crack transecting the upper garnet suggests that it developed due to collision. The arch-shaped foliation domain below the upper garnet exhibits the amount of strain that was taken up by the matrix. The square indicates the location of the element distribution map of Fig. 12. (d) BSE image of cracks in garnet caused by collision. Note that there still is a few micrometer thick contact zone between the garnet grains. The white mica in the contact zone is highly deformed as indicated by the bad polishing.

are depleted (Figs. 6, 7; Wassmann and Stöckhert, 2013b). White mica is the main component of the deformed strain caps and abundant in precipitation sites. Therefore it can be inferred that white mica comprises the main soluble in the matrix. The contact zone is passively enriched in less soluble phases and leaves a residual dissolution seam that is several tens of micrometers wide (Fig. 6a). Dissolution seams are commonly rich in graphite and show a substantial increase in rutile (Fig. 6c). Yet, the solubles are not entirely removed so that white mica is still present in these seams. White mica often exhibits retrograde overgrowth by chlorite in dissolution seams. Overgrowth of chlorite is not only present in these areas but appears more often than compared to other areas. Increased fluid flow in areas of densely spaced foliation planes gives a possible explanation for this observation (Abu-Alam and Stüwe, 2011). Because of the dissolution seam, garnet-garnet contacts are not established. This extend of convergence may be denoted as collision even though the grains do not touch each other directly. The collision of garnets causes two styles of response: (i) fracturing of the grains and (ii) dissolution of garnet (Figs. 6, 7). Cracking of garnets occurs from micrometer (Fig. 7d) to millimetre scale (Fig. 7c) and is ubiquitous in the samples. Dissolution of garnet is not as common as cracking but three sites were identified undoubtedly. The difficulty here is to find proof for mass transfer that must have occurred. One way of determining that dissolution took place is to identify typical geometrical patterns such as indentation of grains (Figs. 7a, b and c) or stylolites (Gratier et al., 2013; Fig. 6c). This, however, may not always be possible. The truncation of chemical zonings unambiguously reveals that deformation happened due to dissolution precipitation creep (Wassmann and Stöckhert, 2013a). More precisely, the first step - dissolution - is recorded in the microstructure. The here studied example shows the truncation of a Mg-rich rim by the indentation of another garnet crystal (Fig. 12). The indented garnet crystal is transected by a $100 - 150\,\mu m$ wide crack that origins near the garnet-garnet contact at the dissolution site. The rims on either side of the cracks exhibit a peculiar composition that is described in a later section (12).

DIVERGENCE Separating movement of garnets relative to another results in a range of different fabrics. Most commonly, cone-shaped strain shadows are linked between two or more adjacent garnets. In places, this leads to in-series-arrangement of strain shadow – garnet – strain shadow successions parallel to the X axis of finite strain (Fig. 8a). Trails of spherical micron-sized fluid inclusions often appear in SS domains. They exhibit a planar geometry and are parallel to the boundaries of neighbouring porphyroblasts. Garnet polycrystals separate along their former grain boundaries (Fig. 8d). Corresponding cracks are preferentially oriented perpendicular to X (Fig. 8e). Still, any other orientation is represented as well. The associated cracks are sealed with minerals of the SS assemblage (Fig. 8).

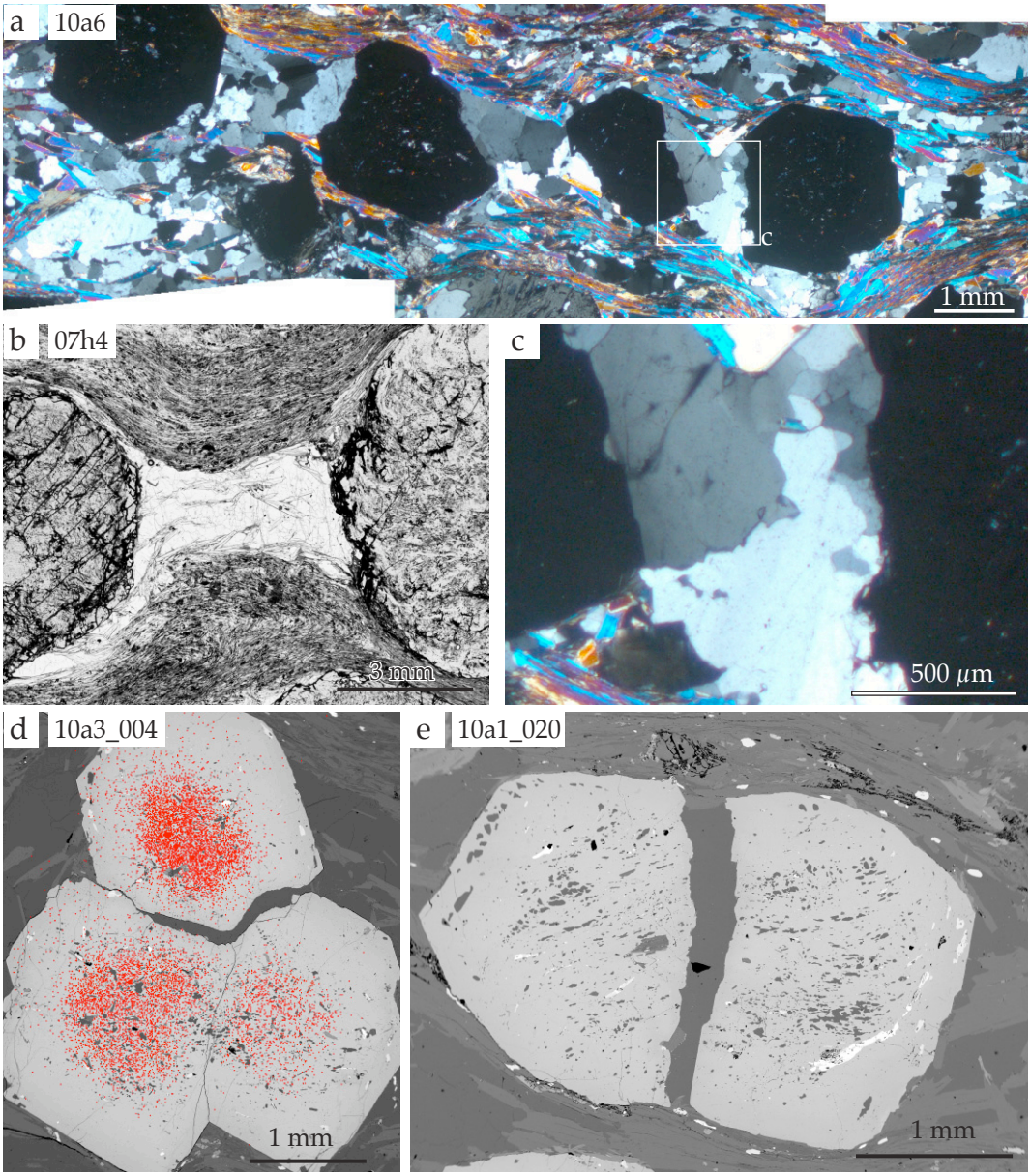

Figure 8: Microstructures that developed as a consequence of garnet divergence. Image labels in upper left corners. (a) Stitched image of four optical micrographs (crossed polarisers) depicting in-series linking of strain shadows between garnets. The square indicates the position of sub-figure c. (b) Scanned thin section of linked strain shadow between two garnets. (c) Detail of sub-figure a depicting grain-boundary-parallel inclusion trails indicative of crack and seal. (d) BSE image with an overlay of a Mn distribution map. The image shows a polycrystal garnet cluster with Mn-rich zones indicating the cores of the garnets. Separation of the cluster occurs at the grain boundaries of the individual garnet crystals. (e) BSE image exhibiting preferential separation of garnet clusters parallel to X, leading to fracturing parallel to Z. Note how well planar Zone-(i)-fabrics match. Note as well, aligned tutile inclusions in the rim of the right grain indicate that this part of the garnet overgrew a strain cap, whereas today this part is adjacend to a strain shadow.

5 PETROLOGICAL ANALYSIS

5.1 CHEMICAL COMPOSITION

Quantitative analysis of the composition of minerals was done for each of the microstructural domains, respectively. The aim was to resolve potential differences in chemical composition. The results of Electron microprobe (EMP) analysis are presented in the following.

GARNET Almandine is the main component in garnet. The end-member fractions are $X_{alm} \sim 0.65 - 0.74$, $X_{grs} \sim 0.11 - 0.21$, $X_{prp} \sim 0.03 - 0.19$ and $X_{sps} \sim 0 - 0.07$. Garnet exhibits compositional zoning that is discussed in a dedicated section (5.2).

WHITE MICA Mainly there are two types of white mica, K-white mica and Na-white mica. Analyses of K-white mica yielded a composition of phengite with $X_{ms} \sim 0.68 - 0.76$, $X_{pg} \sim 0.17 - 0.26$ and $X_{cel} \sim 0.03 - 0.12$ (Fig. 9c). In the XMg - Si (p.f.u.) plot, a linear trend is exhibited. Low XMg ~ 0.5 correspond to low Si (p.f.u.)~ 3.05, high XMg ~ 0.75 correspond to high Si (p.f.u.)~ 3.12 (Fig. 9d). It is worth highlighting that the analyses of phengite in dissolution and precipitation sites show the same scatter.

However, the analyses conducted for white mica were troubled by Na-Si interdiffusion. That is why the obtained data for Na-white mica does not plot in the ternary diagram ms-pg-cel. Hence, Na-white mica is assumed to be represented by the paragonite end-member plus margarite component.

BIOTITE Biotite has XMg$\sim 0.5 - 0.62$, Si (p.f.u.)$\sim 2.65 - 2.9$ and Ti (p.f.u.)$\sim 0.05 - 0.12$ (Fig. 9e). Similar to phengite, no chemical variations in the different microstructural domains are recorded. Note, however, that biotite is only present in precipitation sites. Thus, there are no chemical deviations between MZ and SC domains.

CHLORITE The composition of chlorite is fairly homogeneous. The end-member fractions are $X_{clc} \sim 0.55 - 0.61$, $X_{ame} \sim 0.29 - 0.41$ and $X_{sud} \sim 0.02 - 0.15$. XMg$\sim 0.53 - 0.6$ plots against Si (p.f.u.)$\sim 2.59 - 2.7$.

FELDSPAR Plagioclase is homogeneously Na-rich. It is solely present in SC domains. The end-member fractions are $X_{ab} \sim 0.67$ and $X_{an} \sim 0.33$ (Fig. 10a).

K-feldspar which exists as inclusions in garnet has end-member fractions of $X_{or} \sim 0.98$ and $X_{ab} \sim 0.02$ (Fig. 10a). The composition of K-feldspar is homogeneous.

Sample	10a3			15c		
	core	int.	rim	core	int.	rim
Analysis no.	89	2	50	5	48	110
SiO_2	37.28	37.61	38.36	36.71	37.12	37.18
TiO_2	0.12	0.12	0.04	0.03	0.08	0.04
Al_2O_3	21.16	21.42	21.97	20.91	20.94	21.35
FeO	29.17	31.89	28.76	32.06	33.53	30.43
MnO	3.73	0.32	0.15	3.17	0.50	0.19
MgO	1.16	2.03	4.94	0.92	1.26	4.83
CaO	7.95	7.36	6.62	6.49	7.24	5.49
Total	100.57	100.74	100.85	100.29	100.68	99.50
Si	2.98	2.99	2.98	2.97	2.98	2.95
Al^{IV}	0.02	0.01	0.02	0.03	0.03	0.05
Al^{VI}	1.98	1.99	2.00	1.96	1.95	1.95
Ti	0.01	0.01	0.00	0.00	0.01	0.00
Fe^{3+}	0.02	0.00	0.00	0.04	0.04	0.05
Fe^{2+}	1.93	2.12	1.87	2.13	2.21	1.97
Mn	0.25	0.02	0.01	0.22	0.03	0.01
Mg	0.14	0.24	0.57	0.11	0.15	0.57
Ca	0.68	0.63	0.55	0.56	0.62	0.47
T(3)	3.00	3.00	3.00	3.00	3.00	3.00
M(2)	2.00	2.00	2.00	2.00	2.00	2.00
C(3)	3.01	3.00	3.00	3.02	3.01	3.02
almandine	0.64	0.70	0.62	0.71	0.73	0.65
spessartine	0.08	0.01	0.00	0.07	0.01	0.00
pyrope	0.05	0.08	0.19	0.04	0.05	0.19
grossular	0.22	0.20	0.18	0.17	0.18	0.13
andradite	0.01	0.01	0.00	0.02	0.02	0.03
Total	1.00	1.00	1.00	1.00	1.00	1.00
XMg	0.07	0.10	0.24	0.05	0.06	0.23

Table 1: Selected analyses of garnet for core, intermediate (int.) and rim. Mineral formula calculation on the basis of $12\,O$. Fe^{3+} is estimated by iteration until the ratio $Fe_2O_3/FeO = 2$. The calculation is based on the structural formula $C_2M_2T_3O_{12}$. The lines T(3), M(2), C(3) display how much this site is occupied, the numbers in parentheses are the optimum occupancies . $XMg = Mg/(Mg + Fe)$.

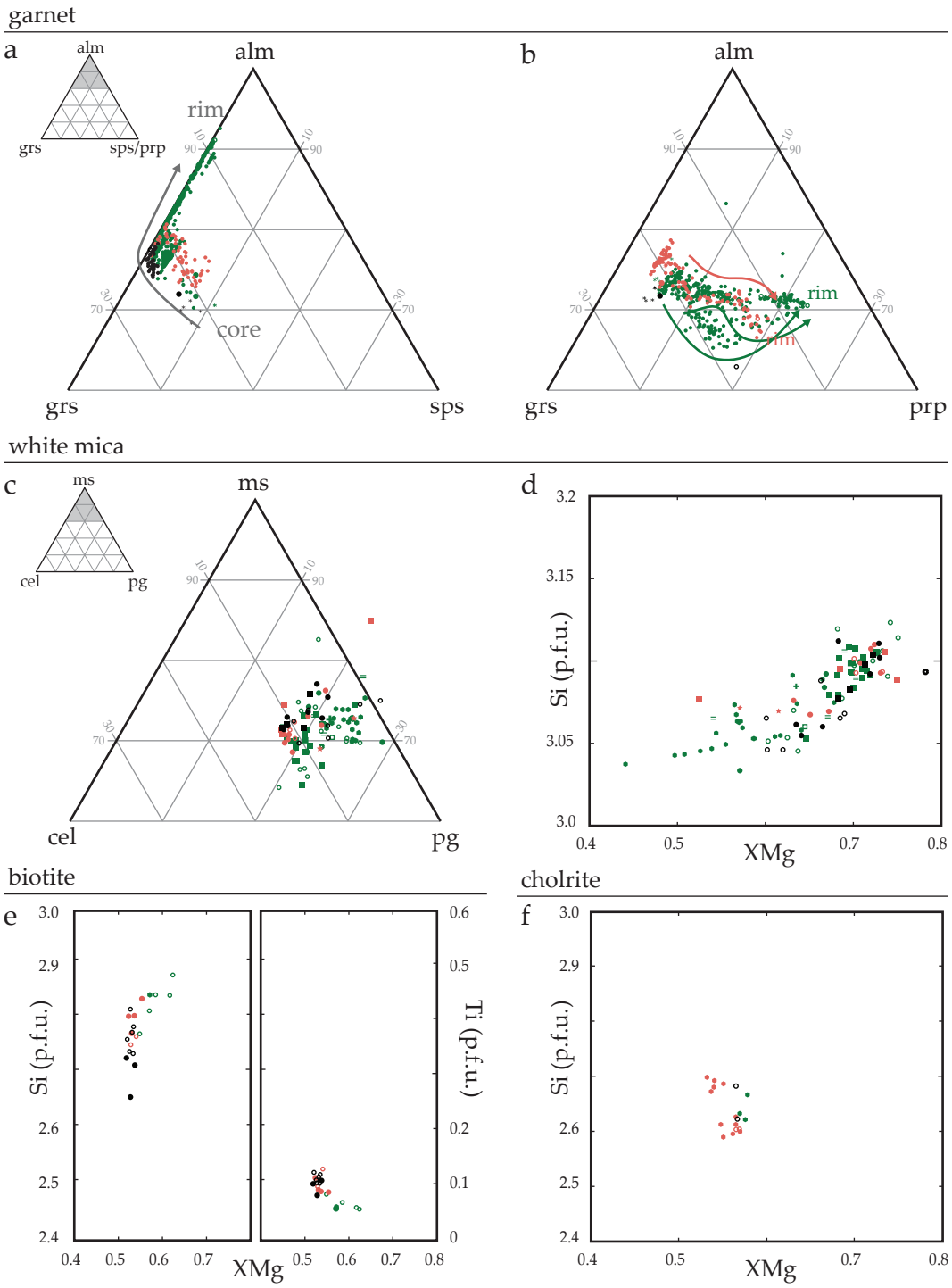

Figure 9: Plots of the mineral compositions calculated from quantitative chemical analysis. The symbols represent the different microstructural domains at which the analysis was done. Colours display different samples. For the key please see Fig. 10b. (a) Garnet composition plotted in the ternary diagram grs-alm-sps. The arrow indicates the trend from core to rim in all data sets. (b) Garnet composition plotted in the ternary diagram grs-alm-prp. The arrows indicate the respective trends of three different profiles. (c) Phengite composition plotted in the ternary diagram cel-ms-pg. (d) XMg – Si (p.f.u.) plot of phengite. (e) XMg – Si (p.f.u.) and XMg – Ti (p.f.u.) plots fo biotite. (f) XMg – Si (p.f.u.) plot fo chlorite.

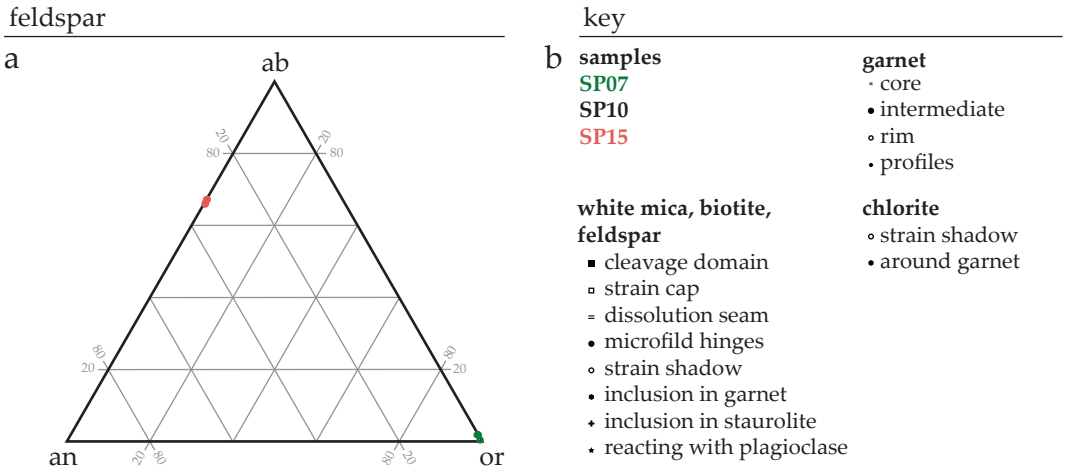

Figure 10: (a) Feldspar composition plotted in the ternary diagram an-ab-or. (b) Key for figures 9 and 10.

5.2 COMPOSITIONAL VARIATIONS IN GARNET

Garnet shows a pronounced concentric growth zoning around the core. In order to representatively characterise the compositional zoning in garnet, an undeformed garnet crystal from sample 15c was analysed. The garnet is circa 1.4 mm in diameter (Fig. 11). A distinctive bell-shaped distribution indicates the highest Mn-concentrations near the core (Fig. 11). The spessartine component near the core is $X_{sps} = 0.07$ and decreases to $X_{sps} \sim 0$ circa 150 µm before the rim is reached. Almandine is the prevailing end-member of garnet with $X_{alm} = 0.70$ in the core. A gradual increase to $X_{alm} = 0.73$ occurs towards the outer core at circa 150 µm distance from the rim. From that point, the FeO content decreases to $X_{alm} = 0.65$ at the rim. The grossular component displays a flat profile at approximately constant $X_{grs} = 0.19$. 100 µm from the rim, the onset of a decrease is exhibited that stabilises on a plateau of $X_{grs} = 0.14$ at circa 50 µm distance from the rim. The pyrope content displays a slight increase from $X_{prp} = 0.04$ to 0.06 mol-% towards the outer core. A change in slope can be observed in the profile that indicates a steeper increase of pyrope component to $X_{prp} = 0.19$ at the rim. The kink in slope coincides with the change in almandine component at circa 150 µm distance from the rim.

SPECIAL FEATURES OF GARNET COMPOSITION The aforementioned change in pyrope content towards the rim is developed ubiquitous in the studied samples. The Mg-rich zone is, however, not restricted to grain boundaries. Some fractures in garnet show a similar increase of Mg content towards the cracks (Figs. 11, 12). The profile shown in Fig. 12 depicts a bell shaped increase of pyrope content from $X_{prp} = 0.06$ towards $X_{prp} = 0.15$ at the crack. A concomitant decrease in Fe is recorded. The almandine content decreases from $X_{alm} = 0.71$ in the distal part to $X_{alm} = 0.65$ in the proximity of the crack. The change in composition is accommodated over a distance of circa 100 µm towards both sides of the crack. No significant changes in X_{grs} and X_{sps} are observed. The accompanied increase

	image	L [µm]
rim	10a1_001	200
		280
	10a1_007	172
	10a1_016	158
	10a1_021	212
		272
	10a2_002	219
crack	10a1_021	59
		49
		39
		64
	10a1_027	33
	10a2_003	23
		38
		33

Table 2: Measurements of lengths of the Mg-enriched, Fe-depleted zones at rims and around cracks in garnet. The sample numbers correspond to the labels in Fig. 13.

in Mg with decrease in Fe both cause a darker z-contrast in BSE images. Therefore, BSE imaging at the highest possible contrast visualises these zones darker than the rest of the garnet (Fig. 13). This method allows for much faster imaging of these zones than the creation of element distribution maps. Hence a larger number of garnets was analysed to investigate these Mg-enriched, Fe-reduced zones. High-contrast BSE imaging revealed that the width of the these zones is variable. Mostly, the wider zones are found at grain boundaries and narrower zones round fractures in interior parts of garnet (Fig. 13).

Another type of garnet composition is depicted by element distribution maps in the vicinity of the adjacent crack near the site of garnet dissolution in sample 07g (Figs. 12a and b). A narrow rim of $40 - 65\,\mu m$ width on either side of the crack exhibits a composition that deviates from the rest of the garnet. Over the distance of just a few micrometers the almandine content increases from $X_{alm} = 0.64$ to $X_{alm} = 0.70$, the pyrope content rises from $X_{prp} = 0.15$ to $X_{prp} = 0.20$, whereas the grossular content decreases from $X_{grs} = 0.18$ to $X_{grs} = 0.08$. The spessartine content stays unaffected. The composition of this rim will be referred to as overgrowth composition in the following. The above described Mg-increase and Fe-decrease is, however, developed at this site as well. The width of the Mg-enriched, Fe-depleted zone varies between 60 and 110 µm from the edge of the overgrowth domain.

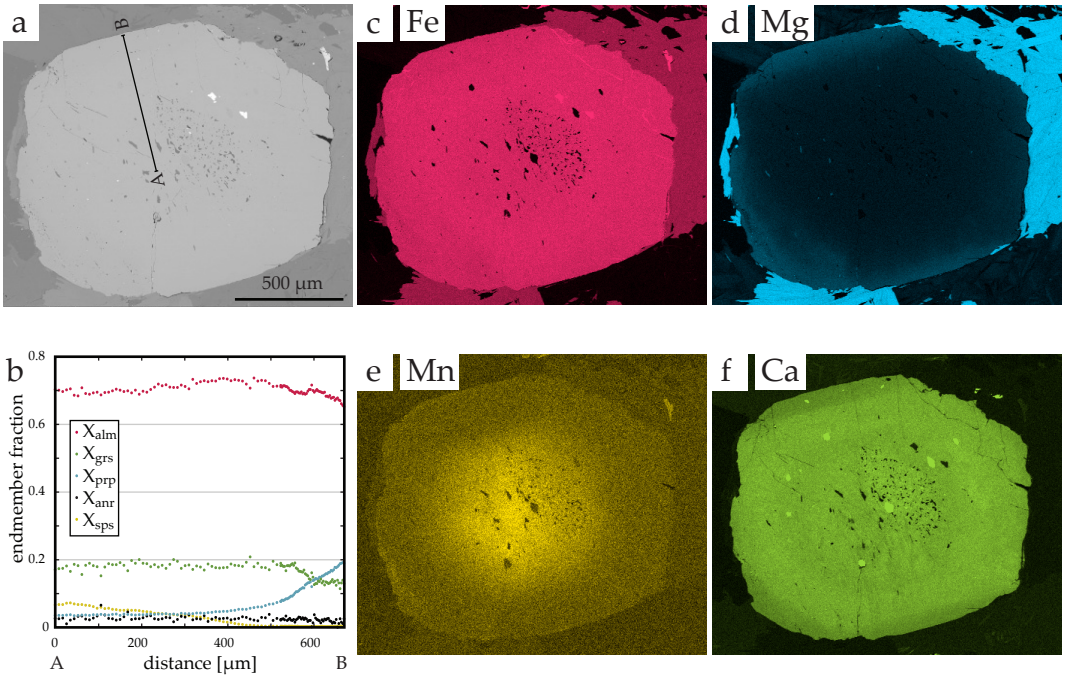

Figure 11: (a) BSE image of a single, undeformed garnet from sample 15c. The line indicates the position of the profile shown in sub-figure b. (b) Profile from core to rim of the garnet crystal. For description see text. Colours of end-members are the same as in the element distribution maps in c-f. (c-f) Element distribution maps of Fe, Mg, Mn and Ca of the areas shown in a. Note the truncation of the Mg-rich rim by chlorite growing at the expense of garnet in sub-figure c.

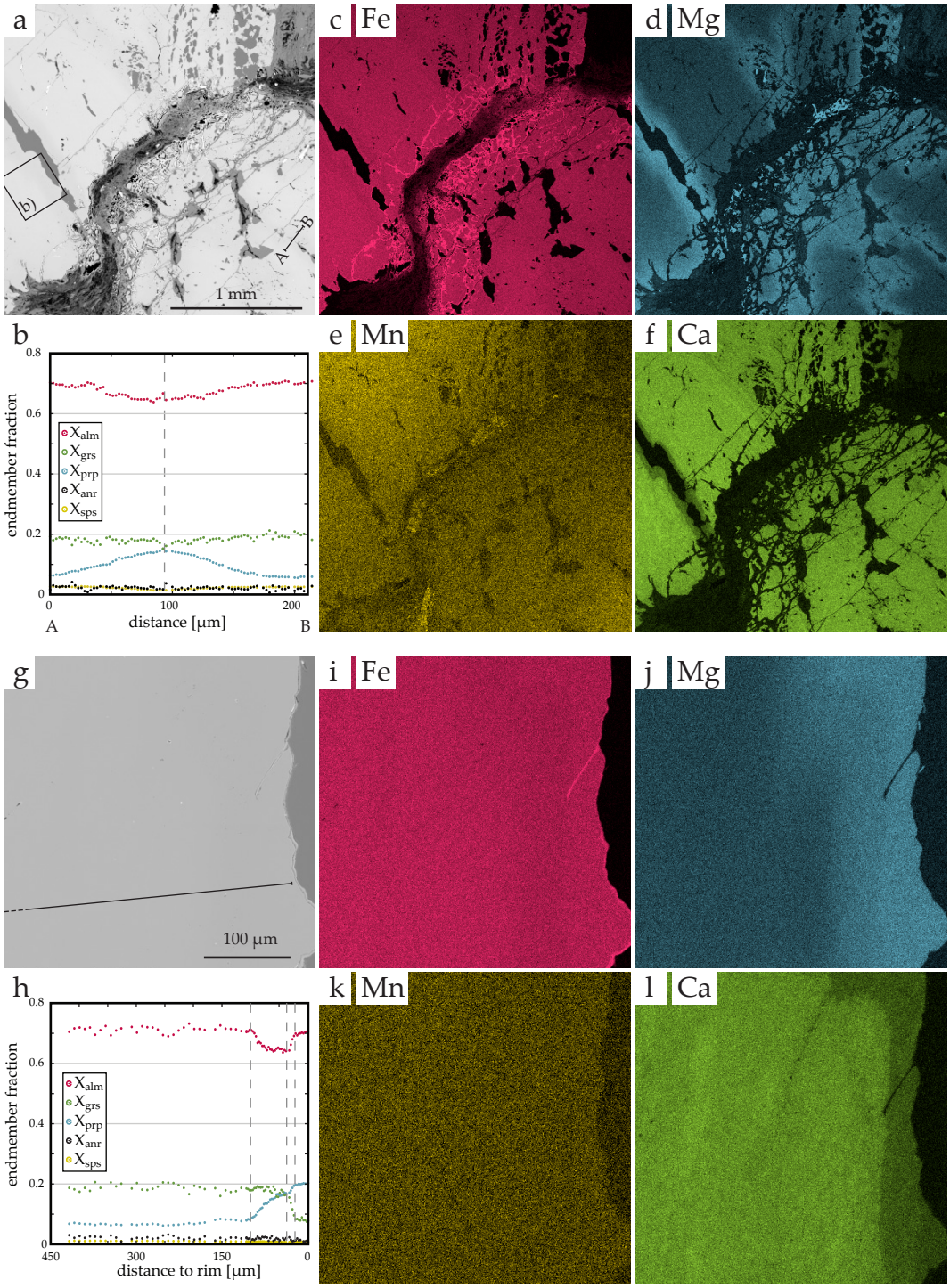

Figure 12: (a) BSE image of a site of garnet dissolution in sample 07g. The line indicates the position of the profile shown in sub-figure b. The square indicates the position of sub-figure g. (b) Profile over a crack with adjacent increase of Mg. For description see text. Colours of end-members are the same as in the element distribution maps in c-f. (c-f) Element distribution maps of Fe, Mg, Mn and Ca in the area shown in a. (d) Note the truncation of the Mg-rich rim of the upper garnet by the indentation of the lower one. NE-SW oriented cracks in the image show enrichment of Mg in their vicinity. (f) Note the Ca-poor domain on either sides of the crack transecting the upper garnet. (g) Zoom-in of a. The line indicates the position of the profile shown in sub-figure h. (h) Profile from the wall of the crack towards the interior of the garnet crystal. Colours of end-members are the same as in the element distribution maps. (i-l) Element distribution maps of Fe, Mg, Mn and Ca in the area shown in g. (i) The narrow ($\sim 50\,\mu m$) Fe-rich rim which is exhibited in the profile h is faintly displayed. (j) The Mg-rich zone extends $\sim 120 - 180\,\mu m$ towards the interior of the garnet. Yet, the step which indicated an increase in Mg towards the rim is weakly marked. (l) The sharp decrease in Ca that is shown in profile h is distinct.

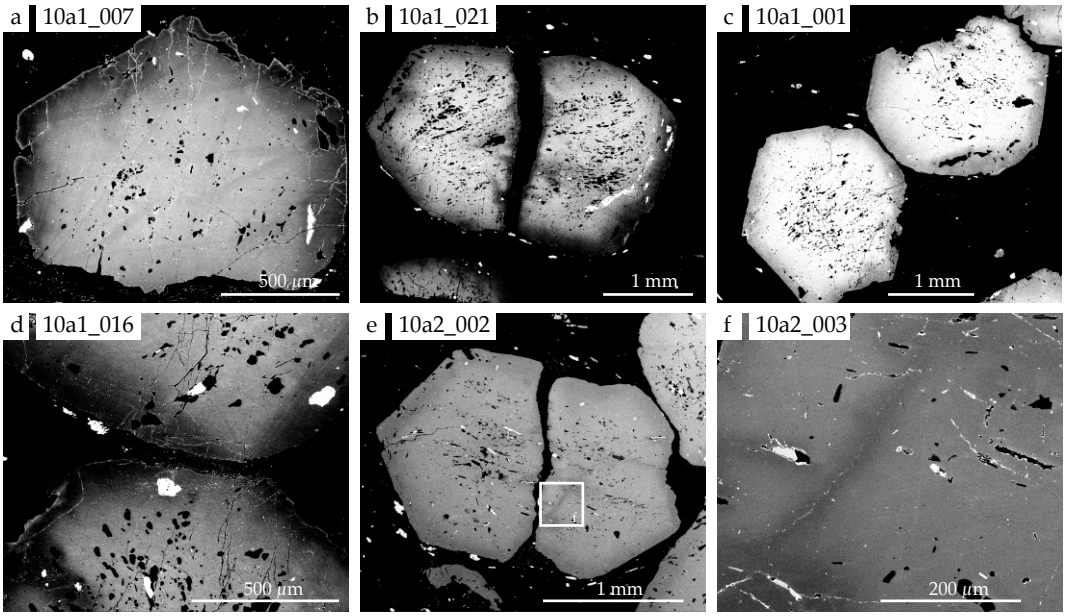

Figure 13: (a-f) High-contrast BSE images showing dark zoning at rims of crystals and around cracks. These zones can be correlated with Mg-increase and concomitant Fe-decrease resulting in a dark appearance in z-contrast images. Image labels in upper left corners.

Part III

DISCUSSION

6

SPACIAL DISTRIBUTION OF THE GARNETS

The spacial arrangement of the garnet crystals was investigated quantitatively in order to get an objective characterisation of the garnet distribution. Therefore quantitative investigation was carried out on (i) the area fraction ϕ of garnet in the sample, (ii) the grain size distribution and (iii) the extent of clustering of grains relative to a completely random distribution. Especially the extend of clustering is of special interest because it is critical for estimating strain from particle distribution (see 10.1).

Sample 15d was chosen for analysis because of the high number of garnets within the thin section. Compared with the garnet crystal size in the rest of the study area, the crystals are relatively small ($\sim 1.2\,mm$ in diameter) in the investigated sample 15d. To analyse the sample, the outlines of the garnet grains were outlined as described in the Methods Chapter (see chapter 3). Clusters of multiple garnets were traced as single grains. The procedures that were applied require a largely homogeneous distribution of grains in all parts of the studied area. Therefore, the study sector was tested for deviations from an equal count of garnets per quadrant using the χ^2 test (Kretz, 2006). The number of grains *in* the selected rectangle is $N = 932$. However, for computing the nearest-neighbour distances, the study area had to be extended because some of the grains close to the boundary have their nearest neighbour outside the study area. Therefore, some grains outside the selected area had to be considered as well. Hence the number of *all* grains is $N_0 = 937$.

6.1 TEST FOR DEVIATIONS FROM EQUAL COUNTS PER QUADRANT

The χ^2 test was performed following the now described procedure (Kretz, 2006). The study area was divided into four quadrants. For each, the number of garnet grains was computed using the command Analyze Particles in Fiji. Grains which are located on the boundaries of the quadrants were classed with the quadrant in which the majority of their area is. The figure χ^2 was reckoned using the equation:

$$\chi^2 = \frac{\sum_i (N_i - N_q)^2}{N} \tag{1}$$

where N_i is the number of grains in a quarter, N is the number of grains in all quadrants and $N_q = N/4$, the average number of grains in a quadrant. The computed figure is then compared to a critical value. A low deviation from N_q is confirmed for values of $\chi^2 < 7.8$ (Kretz, 2006). The calculation of χ^2 with:

$N_1 = 259$
$N_2 = 234$
$N_3 = 210$
$N_4 = 229$
$N_q = 233$

gives $\chi^2 = 1.31$. The above mentioned criterion is thus confirmed for the selected area. Consequently, further testing can be carried out.

6.2 AREA FRACTION ϕ

The area fraction ϕ describes the area fraction of garnets in a two-dimensional plane. ϕ was computed by pixel counting. The command histogram in Fiji provided the counts for garnet grains (black, value = 0) and matrix (white, value = 255). Using the equation

$$\phi = \frac{A_{grt}}{(A_{grt} + A_{matrix})} \tag{2}$$

where A_{grt} is the area of garnet, A_{matrix} is the area of matrix minerals. Plugging in the values gives $\phi = 0.186$.

6.3 GRAIN SIZE DISTRIBUTION

As explained above, there are certain issues which have to be considered when studying three dimensional phenomena in only two dimensions. One such aspect is the study of grain size distributions, where grain size is plotted against frequency. First, defining the quantity of grain size is important. There are a number of possible ways to define the size of a grain. However, the volume V and the cross sectional area A of a grain are well suitable measures because they are independent from the shape of the grain (Heilbronner and Barrett, 2014). In the course of this study, I decided on examining the grain size distribution based on the area for three reasons: (i) the area fraction of a phase i in a sectional plane is approximately equal to the volume fraction of that phase (eq. 11; Heilbronner and Barrett, 2014). (ii) Garnet crystals are close to spherical. When randomly cutting a sphere, the sectional circle will most probably have a radius r close to the radius R of the corresponding sphere. The likelihood that r is larger than $0.5R$ is 87%. Thus, determining the radii of sectional circles will, most likely, yield values which are only slightly smaller than the radii of the cut spheres (Heilbronner and Barrett, 2014). (iii) Although there is no proportionality between 2-D and 3-D grain size distributions, it is feasible to deduce a *possible* distribution of spheres for any distribution of sectional circles (Heilbronner and Barrett, 2014). However, the procedure is quiet sophisticated and causes another source of error.

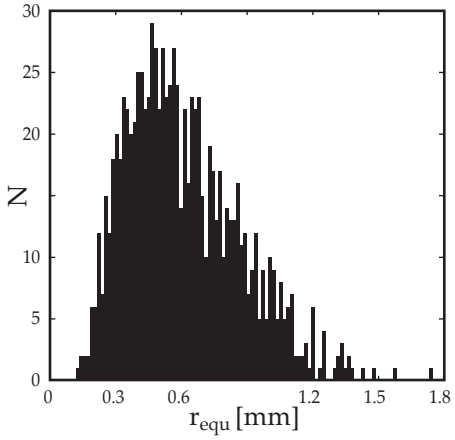

Figure 14: Frequency plot of the grain size distribution of sample 15d. The bin size is 16.67 μm.

The area of a grain can be determined easily using the particle analyser of Fiji. The equivalent radius r_e of an area-equivalent circle for each grain will be used to characterise the grain size. r_e is given by:

$$r_e = \sqrt{\frac{A}{\pi}} \tag{3}$$

where A is the area of a grain (Heilbronner and Barrett, 2014). The histogram of the grain size distribution is shown in Fig. 14.

6.4 SPACIAL DISTRIBUTION PATTERN

The qualitative microstructural study of the various samples from the Steinplan area conveyed the subjective impression that the garnets have a clustered distribution. Therefore, the aim is to quantify the physical configuration of the garnet grains. In order to objectively describe the spacial distribution pattern, two similar approaches were applied: (i) the method of Kretz Kretz, 2006 and (ii) the method of Jerram et al. (1996). Both methods compare the mean minimum distances between an object and its nearest neighbour in a sample with a random distribution. Either use the same procedure to determine the nearest neighbours (Clark and Evans, 1954). The differences between the approaches are the following. In the first procedure, the nearest-neighbour distances are measured from rim to rim. In contrast, centre-to-centre nearest-neighbour distances are used in the second procedure. Furthermore, the frequency of grains is defined as objects per area for method (i) and as area fraction of objects for method (ii).

6.4.1 *Spacial analysis after Kretz (2006)*

The rim-to-rim nearest-neighbour distances were determined using using digital image analysis. A Fiji Macro (written by M. Voorn) was used in order to perform the following steps automatically:

1. Increase the size of the canvas to prevent edge effects.

2. Run Local Thickness plug-in (Dougherty and Kunzelmann, 2007). The Local Thickness plug-in attempts to fit spheres of the largest possible diameter between two contrasting regions in any image. For every successfully fitted sphere, all pixels within this sphere get a value equal to the sphere diameter. By letting the plug-in fit spheres in the space between particles, a measure for the particle spacing is obtained, at every pixel in the image.

3. Label separate particles in the input image, using a Particle Analyzer (Doube et al., 2010).

4. Determine the values for particle spacing in the direct vicinity of a particle: on the result from the Local Thickness plug-in, extend each original particle by a few pixels (command Dilate) and delete the original particle (command Erode).

5. Record the minimum value for particle spacing within the realm determined at step 4.

The output gives a list of the nearest-neighbour distances d_S for each grain in pixels. Converting the data in millimetres was done by multiplying with:

$$\frac{sample\,width[mm]}{sample\,width[px]}$$

Next, the mean $\bar{d_S} = 0.406\,\text{mm}$ was calculated. The mean distance between randomly distributed grains d_R is given by:

$$d_R = \frac{1}{2}\sqrt{\frac{N}{A}} \tag{4}$$

where A is the area of the study area. Plugging in the respective values gives $d_R = 1.328$. The comparison between $\bar{d_S}$ and d_R is given by the ratio R and calculates:

$$R = \frac{\bar{d_S}}{d_R} \tag{5}$$

Values close to 1.0 represent random distribution, small R refer to clustering and large values up to $R = 2.15$ stand for regularity. The here calculated $R = 0.306$ is significantly smaller than $R = 0.5$ which indicates highly clustered distributions (Fig. 4 in Kretz, 2006). However, the here studied garnet distribution is not that highly clustered, although the calculated R is even smaller than the boundary value of Kretz' method. A possible cause for this deviation is the different fraction of garnet (<5% in the samples studied by Kretz (2006) versus ca. 19% in this study). With increasing area fraction of grains the described method loses applicability (Kretz, 2006). Hence, this way of describing the distribution pattern is inappropriate. Thus, the second approach was carried out as described below.

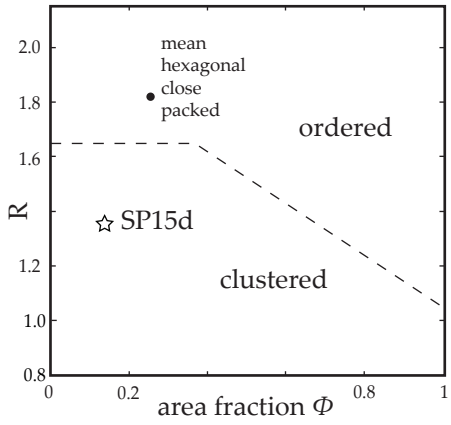

Figure 15: Plot showing the degree of clusteredness R in dependance of the area fraction ϕ. The dashed line separates the fields of clustered and ordered distributions. The star indicates the studied sample. (Modified after Jerram et al., 1996, Fig. 5)

6.4.2 *Spacial analysis after Jerram et al. (1996)*

The determination of d_S is readily performed using the command Analyze Particles implemented in Fiji. The arithmetic mean $\bar{d_S} = 1.608\,\text{mm}$ was computed. The mean distance for random distributed points is defined as follows

$$d_R = \frac{1}{2}\sqrt{\phi} \tag{6}$$

where ϕ is the area fraction of garnet (see 6.2). Plugging in ϕ delivers $d_R = 1.159$. The ratio R of the sample and random distribution is likewise given by Equation (5) and gives $R = 1.388$. In a plot of area fraction ϕ versus R sample 15d plots in the field of clustered distribution (Fig. 15). The computed R-value does not differ as much from random distribution as in the method by Kretz. Considering the particle density appears to be crucial for comparing observed and completely random distribution patterns.

7

RELATIVE TIMING OF DEFORMATION

The relative timing of deformation events can be inferred by the afore described microstructures. The internal fabrics which are preserved in garnet yield the most revealing hints. The earliest recorded stage of deformation event led to the development of a spaced foliation which is preserved as Zone-(i)-fabrics in the interior of garnet crystals. Prograde growth of garnets preserved a pre-existing fabric which was lacking strain caps and shadows. Zone-(i)-fabrics may be interpreted in several ways. Strain shadows and caps did not occur due to one or more of the following reasons: (i) the strain rate was too low to initiate a transformation of the matrix surrounding the porphyroblasts. (ii) No fluid was present, i.e. no medium to effectively accommodate diffusional mass transfer was available (Gratier et al., 2013). Or (iii), the temperature was too low to allow for ductile deformation. However, the garnet-in reaction occurred at 480°C. The first explanation is preferred because the presence of garnet suggest high temperatures. Thus, (iii) can be discarded. Secondly, an initial absence of a fluid phase that is followed by a sudden excess in in fluid would need for a strong evidence. No such evidence is observed. The contrary is the case, prograde metamorphism in pelitic rocks is associated with dehydration reactions (Connolly and Thompson, 1989). A sufficient supply of fluid can therefore be assumed rendering the first explanation of a low strain rate during the first deformation the most likely.

Ongoing garnet growth was accompanied with deformation of the host rock, resulting in preservation of folded, sigmoidal and millipede inclusion patterns (Zone-(ii)-fabrics). Whether the succession of the growth of zone (ii) was continuous or discontinuous after the growth of zone (i) cannot be determined. Additionally, some relative movement of the garnets in respect to each other must have occurred in order to obtain the present-day random configuration of planar features. Secondly, strain caps and strain shadows of the presently observed microstructure show continuity in zone (ii) garnet rims (Figs. 5c, d). This means that garnet was still growing at the latest stage of deformation which caused the finite strain pattern. Relative rotation of garnet amongst them, the development of $cr1$ and associated s_m as well as the development of strain caps and shadows is related to change in the style of deformation. Foam-microstructure of quartz inclusions in garnet indicate high temperature low differential stress conditions when garnet growth initiated (Stöckhert et al., 1997). The poikiloblastic overgrowth of strain shadows by garnet preserves the same quartz microstructure. Obtained quartz inclusions in both domains exhibit characteristics of static recrystallisation. The absence of dislocation creep in quartz indicates that low-stress conditions were predominant when strain shadows evolved. Experimental flow laws for quartz can be used to calculate the upper limit for differential stress which yield $2\,MPa$ at $600°C$ (Paterson and Luan, 1990; Stöckhert et al., 1997). The present-day observed features correlating to grain boundary migration dynamic recrystallisa-

tion, therefore, have to be a feature that developed at a later stage. The associated deformation must have occurred more or less successively after the deformation that caused the present-day configuration of matrix and porphyroblasts. Grain boundary migration dynamic recrystallisation is a mechanism acting at temperatures above $500 - 550$°C (Stipp et al., 2002). As, a consequence, the segment on the PT-path along which dynamic recrystallisation of quartz has occurred is constrained between DPC-related deformation and cooling below ~500°C. The latest stage of deformation that is recorded caused $cr2$ crenulation oblique to the l_m and $cr1$. Whether or not dynamic recrystallisation of quartz correlates with this deformation is not evident in the samples.

8

IS THERE EVIDENCE FOR TECTONIC PRESSURE?

Itemising the quantitative mineral analysis appeared as a very helpful tool to recognise that there are no chemical variations across the respective microstructural domains. Mineral compositions do scatter, nonetheless, but variations lie within the same interval for the different domains. This observation is valid for phengite, feldspar, biotite and chlorite. However, the implications that can be drawn from phengite are most extensive because phengite occurs syn-deformational in strain caps as well as in strain shadows. Strain caps develop in the fields of incremental shortening where the largest differential stresses occur around a porphyroblast. Strain shadows develop in the fields of incremental stretching where the lowest differential stresses occur around a porphyroblast. Numerical models predict pressure variations in these domains (Schmid and Podladchikov, 2003). Variations in lithostatic pressure that are the result of deviations in stress are also referred to as tectonic pressure which is a highly debated topic (Mancktelow, 2008, and references therein). Positive variations in pressure, also called overpressure, would therefore be expected in strain caps. Negative pressure variations or underpressures would be expected in strain shadows. Phengite is present at sites of convergence (strain caps) and divergence (strain shadows) and thereby in potential areas for deviations from lithostatic pressure. Owing to the P-dependance of Si-content, phengite constitutes an adequate geobarometer (Massonne and Schreyer, 1987). Nevertheless, since there are no deviations in Si between strain caps and strain shadows, it can be concluded that no local differences in pressure were recorded. This does not necessarily mean that pressure variations were never obtained during the deformation of the rocks. Stress anisotropies cause differences in chemical potential which are considered as the driving force of dissolution precipitation creep (Wheeler, 1992; Gratier et al., 2013). The chemical potential of a phase is high at the site of high differential stress, as compared to a site of low differential stress. The resulting gradient in chemical potential causes diffusion from the former to the latter site. Another driving mechanism are electrochemical potential differences that emerge between two distinct phases. This effect controls the dissolution of one of these phases, which has been shown experimentally by Greene et al. (2009). That phase boundaries play an important role in facilitating dissolution precipitation creep has also been highlighted by Wassmann and Stöckhert (2013a). Hence, pressure deviations do not have to be high in order to drive dissolution at the loaded interface. The fact that phengite does not record any significant variation in Si, and thus in pressure, strengthens these findings. Even more peculiar from this point of view is the observed fracturing of garnet across thin seams of phyllosilicates (Fig. 7). Cracking of garnet requires the crystals to be linked at least mechanically, if they do not touch. Of course, assuming perfect spheres, this contact would only be a point and accordingly unlikely to be contained in a thin section. However, the

samples consistently show that garnets converge up to minimum distance which is often characterised by a seam of phyllosilicates, graphite and other accessory minerals of similar thickness. Therefore, considerable stress transfer must have occurred over these gaps in between garnets for allowing fracturing of crystals to happen. Three possibilities could explain why the present-day composition of phengite does not reflect this: (i) prior to garnet fracturing, when the differential stresses were still high, the composition adapted to the associated deviation in lithostatic pressure. After breaking and relaxation, the phengite re-equilibrated. (ii) The event causing relative increase in pressure are too short for adjusted phengite compositions to accomplish. This means, the reaction rate of phengite to achieve a stable composition for the corresponding pressure is too low (Massonne and Schreyer, 1987). (iii) The presence of a fluid phase, which is evident because of the DPC-specific microstructure, causes rapid equilibration of phases as soon as incremental differences in compositions occur. The latter and the second possibility constitute two processes which can be reasonably assumed to act concomitantly. However, even though phengite crystallises newly in SS domains and therefore does not need to equilibrate, no compositional variations are recorded. Hence, phengite cannot be used to asses potential deviations in lithostatic pressures in these rocks.

9.0.3 *Calculation of equilibrium phase diagrams*

Equilibrium phase diagrams were modelled using the THERIAK-DOMINO programme collection (deCapitani and Petrakakis, 2012; deCapitani and Petrakakis, 2010). The modelling was done in the system MnNCKFMASTH. The database tc325 (Holland and Powell, 1998) was used with minor modifications. The employed activity models for the following minerals are given in parentheses: garnet, staurolite and cordierite (Holland and Powell, 1998), white mica (Coggon and Holland, 2002), biotite (White et al., 2007), feldspar (Baldwin et al., 2005). Ilmenite was modelled assuming an ideal solution of ilmenite-geikielite-pyrophanite. For paragonite an ideal solution of margarite-paragonite was assumed because in rare cases paragonite is Ca-bearing. Quartz and H_2O are considered as saturated. The calculations are based on the simplified bulk composition of sample 10. A part of Ca was subtracted to compensate for Ca that is occupied in apatite. The moles Ca that are bound in apatite were computed from the bulk phosphorous-content. The modified bulk composition that was used to calculate the equilibrium phase diagrams is shown in table 3. Additionally, thermodynamic modelling was performed for sample 07. The calculated equilibrium phase diagrams for 07 and 10 resemble each other greatly (for the equilibrium phasediagram of sample 07 please refer to the appendix v). The stability fields for respective stable assemblages plot in very similar PT ranges. Therefore, only the results of sample 10 are presented and discussed in the following.

The fraction of garnet in the studied sample is ~ 0.16. Porphyroblasts in rocks that did not reach granulite facies conditions during prograde metamorphism commonly exhibit compositional growth zoning (Marmo et al., 2002). This suggests that equilibrium between a crystallising porphyroblast and its surrounding matrix could not be obtained during grain growth. As a consequence, element fractionation between porphyroblast and matrix can be assumed (Marmo et al., 2002). Because the here studied samples display compositional zoning in garnet, bulk rock fractionation is expected. The fractionated bulk rock composition was calculated as follows. My approach is to subtract the average composition of garnet inside of the rim of Mg-increase and Fe-decrease. The basic assumption is that garnet constitutes the only sink for Mn. Therefore, the amount of Mn in the whole rock equals the amount of Mn in garnet:

$$N_{Mn}^{bulk} = N_{Mn}^{grt} \tag{7}$$

where N_{Mn}^{bulk} is the Mn-content of the bulk composition in moles and N_{Mn}^{grt} is the Mn-content of garnet in moles. The number of moles of Mn in garnet is given by:

$$N_{Mn}^{grt} = 3\, X_{sps}\, N^{grt} \tag{8}$$

Whole rock analysis		Moles		
	wt-%	N [mol]	bulk	bulk - garnet
SiO_2	51.37	Si	61.42	57.70
TiO_2	0.79	Ti	0.71	0.71
Al_2O_3	28.27	Al	39.83	37.35
FeO	8.12	Fe	8.12	5.48
MnO	0.13	Mn	0.13	0.00
MgO	0.90	Mg	1.61	1.44
CaO	2.03	Ca	2.40	1.62
Na_2O	0.88	Na	2.04	2.04
K_2O	4.05	K	6.18	6.18
P_2O_5	0.12			
$H_2O^{110°C}$	0.20			
H_2O^+	1.44			
CO_2	0.81			
SO_3	0.02			
$Total$	99.13			

Table 3: Table with whole rock analysis raw data on the left. On the right, the simplified bulk and fractionated bulk composition are shown in the respective columns.

where X_{sps} is the end-member fraction of spessartine in garnet and N^{grt} the number of moles of garnet in the rock, which is the unknown variable that is calculated. X_{sps} is the average value of spessartine content in the inner part of the garnet shown in Fig. 11a, taken from the profile across it (Fig. 11b). Rearranging and substituting in equation 7 yields:

$$N^{grt} = \frac{N_{Mn}^{bulk}}{3X_{sps}} \tag{9}$$

Using the average X_{sps} in the interior of the garnet (before Mg-increase and Fe-decrease start) in sample 15c, $N_{grt} = 1.238$ is obtained. The amount of each element in garnet was calculated with:

$$N_i^{grt} = Y_i \, X_{end} \, N^{grt} \tag{10}$$

where N_i^{grt} is the number of moles of element i in the garnet end-member *end*, Y_i is the number of atoms of i per formula unit and X_{end} is the respective end-member fraction of garnet. The so calculated moles of each element were subtracted from the bulk composition (Tab. 3).

9.0.4 *Interpretation of the equilibrium phase diagrams*

The depicted PT-path is constrained by microstructural observations as well as quantitative analyses. Microstructural analysis yielded the following. Chloritoid inclusions are preserved in the interior of garnet. The chloritoid-out reaction at ca. $550°C$ thus sets an upper limit for the onset of garnet growth. The assemblage of the porphyroblastic minerals garnet + kyanite + staurolite is stable in a very narrow field between $575°C$ at 1.05 GPa and $600°C$ at 0.85 GPa. To preserve staurolite, the metamorphic conditions cannot have been much higher. The peak metamorphic conditions are therefore inferred to be $590 \pm 20°C$ and 1 ± 0.1 GPa. The results of quantitative chemical analysis were combined with calculated garnet isopleths. Measured fractions of grossular and pyrope were used in conjunction with isopleths to define intervals in the PT space. Core and intermediate compositions were distinguished in order to consider bulk rock fractionation. Garnet core analyses are plotted with bulk-rock isopleths (Fig. 16b), whereas intermediate compositions were plotted with fractionated-bulk-rock isopleths (Fig. 16e). Overlapping regions display $540 - 560°C$ and $0.7 - 0.9$ GPa for growth of garnet cores (Fig. 16b). Intermediate garnet composition suggests growth at $550 - 580°C$ and $0.8 - 1.0$ GPa (Fig. 16e). Variations in almandine content are not as decisive as variations in grossular and pyrope fractions because almandine is the prevailing component of garnet (pers. comm. Dave Waters). Therefore, it was not taken into consideration for confining an intersection of isopleths. Spessartine was not considered because it is subject to strong fractionation during crystal growth and thus inappropriate for use in equilibrium thermodynamic modelling. For comparing phengite composition and isopleths, only results based on the fractionated bulk composition are feasible to consider. This is because phengite is assumed to be in equilibrium with the fractionated matrix.

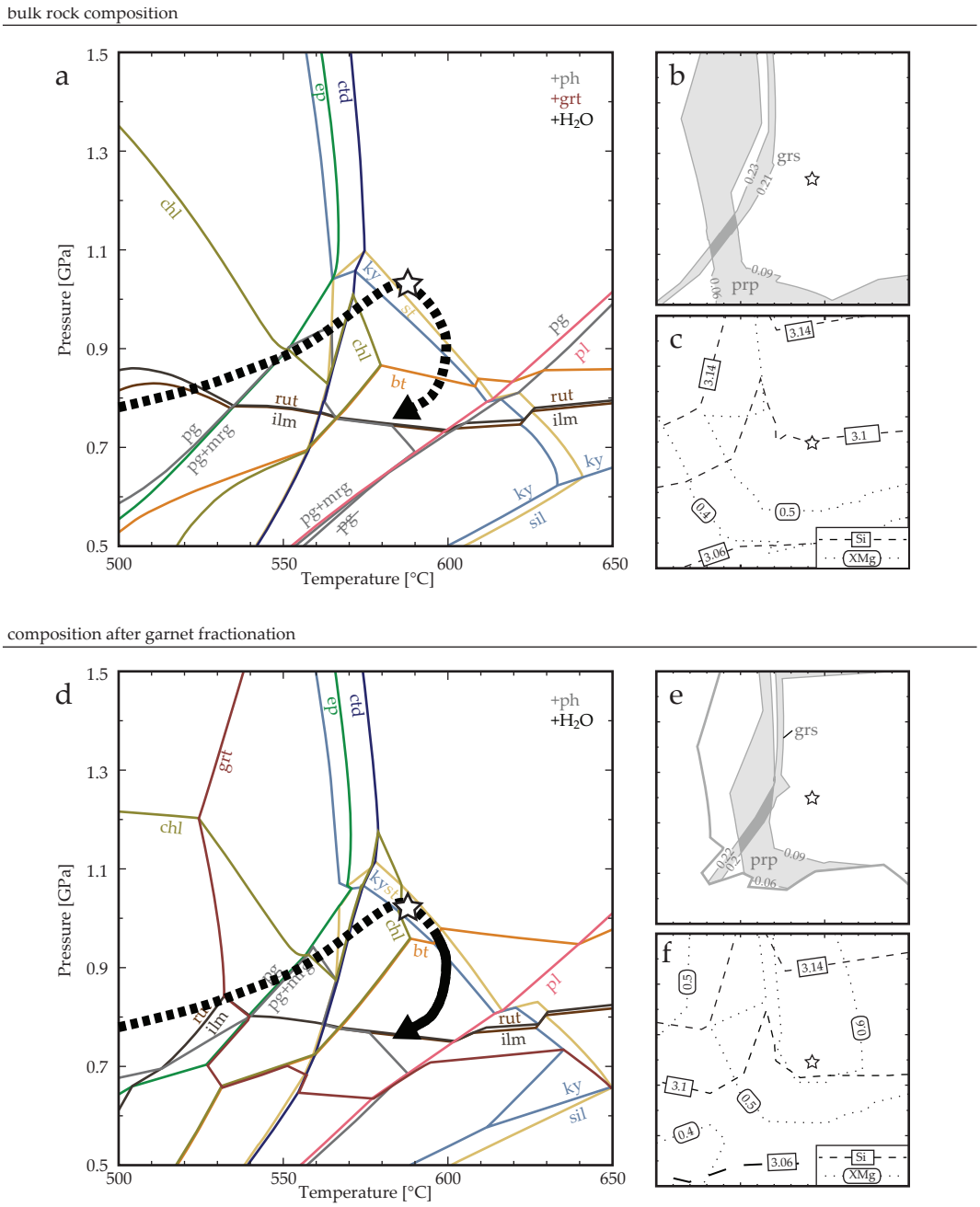

Figure 16: Diagrams showing the results of thermodynamic modelling. grt - garnet, ph - phengite, pg - paragonite, ky - kyanite, st - staurolite, rut - rutile, ilm - ilmenite, pl - plagioclase, sil - sillimanite, bt - biotite, chl - chlorite, mrg - margarite, ep - epidote, ctd - chloritoid. The curves in a and d indicate the in-reactions of minerals whereas the label is on the side where the respective mineral is stable. Colours of labels correspond to the reaction curves. (a) Equilibrium phase diagram for the bulk composition (Tab. 3). (b) Garnet isopleth diagram of X_{grs} and X_{prp} corresponding to sub-figure a. The isopleth intervals depict the measured composition in the core. (c) Phengite isopleth diagram of Si (p.f.u.) and XMg corresponding to sub-figure a. (d) Equilibrium phase diagram for the fractionated bulk composition (Tab. 3). (e, f) Likewise to sub-figures b and c.

The phengite isopleth of Si (p.f.u.)= 3.12 depicts an approximately isobaric trend at P= 1 GPa, except for a narrow peak to ca. 1.2 GPa between $550 - 570°C$. Since the peak is only narrow and, thus, unlikely to represent a trail of the PT-path, phengite isopleths constrain the maximum pressure to ca. 1 GPa.

10 QUANTIFICATION OF STRAIN

10.1 ESTIMATION OF THE FINITE STRAIN ELLIPSE FROM THE DISTRIBUTION OF PARTICLES

Granular microstructures can be used to approximate the finite strain ellipse under certain prerequisites (Ramsay and Huber, 1983). First, if there is more than one type of granular inclusion, the competence contrast has to be negligible. Since only garnets are studied this requirement is fulfilled. Secondly, the initial distribution must not be completely random (Ramsay and Huber, 1983). Why this is important will be explained below. Two approaches are used to estimate the finite deformation from the distribution of garnets: (i) the enhanced Normalised Fry's Method (Erslev and Ge, 1990) and (ii) the delaunay nearest neighbour triangulation method (DTNNM) (Mulchrone, 2003).

The shape of a grain is inappropriate to unambiguously infer finite strain ellipse. That is because initial shape, competence contrast and neighbouring objects influence how a grain deforms. The spacial relationship of grain centroids can, however, be used to estimate the finite strain ellipse (Ramsay and Huber, 1983). Nevertheless, the pre-deformation distribution of the studied objects has to be either anticlustered, i.e. the centres have to be more or less equally spaced (Ramsay and Huber, 1983) or else, clustered. In any case it must not be Poisson random, but diverge from random distribution to either regularity (anticlustering) or clustering (Fry, 1979). Namely, Poisson random distributed points can lie on top of each other or in their immediate vicinity, plus, leave other areas vacant. Such a distribution would not record positive length changes parallel to the instantaneous stretching axis or negative length changes along the instantaneous shortening axis, respectively. Instead, the post-deformation distribution would again be Poisson random (Fry, 1979). The distribution of the garnets in the studied samples is clustered, as shown in sub-section 6.4.2, and therefore appropriate for applying the Fry method.

The method of Fry (1979) compares the locations of one central reference point to every other point of the studied sample. Successively each point is put on top of the reference point and every other point is marked on an overlay (analogue or digital). A central vacancy field surrounded by a high density field of points will develop, if the initial configuration was not random. This approach constituted a big progress in quantitative structural geology due to its fast and easy practice. Still, weaknesses include (i) user-dependent definition of the particle centres (Meschede, 1994) and (ii) ambiguous ellipse-fitting to the Fry plot (Waldron and Wallace, 2007). Advances in the employment of computer-aided data evaluation helped to diminish these deficiencies. Regarding aspect (i), the development of digital image analysis programmes, render an objective definition of centroids possible. Such a tool, the Particle Analyzer of Fiji, is utilised in this study. The

term object is here used in a sense, that the results are reproducible when employing the same software and sample. The centres of grains are per definition the centres of gravity (Ferreira and Rasband, 2010). Concerning point (ii), Waldron and Wallace (2007) developed the so-called continuous function method comparing a trial ellipse with the Fry plot. The best-fit trial ellipse will be used as estimate for the finite strain ellipse.

For the example considered in this study, the centroid distribution is clustered to a certain extend. Therefore, one basic requirement for applying Fry's method is fulfilled. Yet, in the Fry plot, the transition between the inner vacancy field towards the surrounding high-density field of points is rather gradual than sharp, if the degree of anticlustering is low. Thus, ellipse-fitting is hampered (Crespi, 1986). In addition, the variation grain size needs to be considered. Accordingly, a refinement of Fry's technique is done by normalising the centre-to-centre distances by dividing them by the sum of their respective radii (Erslev, 1988). Therewith two crucial advances are achieved: (i) the inner vacancy field is defined more clearly and (ii) the negative impact of clustering of points is minimised, i.e. particles with varying size may be analysed. Erslev and Ge (1990) introduced another advancement, called the enhanced Normalised Fry's Method. Points which lie outside the high-density field of points are eliminated by an user-defined threshold distance. However, Mulchrone (2003) proposed a novel approach, determining the nearest neighbours with Delaunay triangulation. Enhancement (Erslev and Ge, 1990) and Normalisation (Erslev, 1988) of data is also applied. The fitting of the finite-strain ellipse is performed using a steepest gradient nonlinear least squares algorithm (Mulchrone, 2003). Although not decisive in small samples, the advantage of this method lies in its computational effectiveness (Mulchrone, 2003).

In this study, two approaches were utilised to approximate the finite strain ellipse. First, the enhanced Normalised Fry's Method was performed using the Fiji Macro FryJ (Waldron and Wallace, 2007). Subsequently, the generated Fry plot was analysed with Fiji Macro FryJFit (Waldron and Wallace, 2007) to find the best-fit strain ellipse. The procedure revealed an aspect ratio of $R = 1.26$ and angle towards the horizontal boundary of the reference frame of $\varphi = 140.3°$. Hence, the long axis of the calculated strain ellipse is parallel to the foliation.

Secondly, the delaunay triangulation nearest neighbour method was conducted employing the MATLAB function `adtnnm`, implemented in the toolbox PolyLX (Lexa, 2014). Values for the strain ratio of $R = 1.20$ and orientation to the reference frame of $\varphi = 136.93°$ were obtained. Again, the calculated strain ellipse has its long axis parallel to the foliation.

The obtained values are relatively low considering the subjective impression of a highly strained matrix. This could give evidence that deformation is rather accommodated by the matrix than the relative movement of porphyroblasts and that strain is partitioned into the matrix (Ramsay and Huber, 1983).

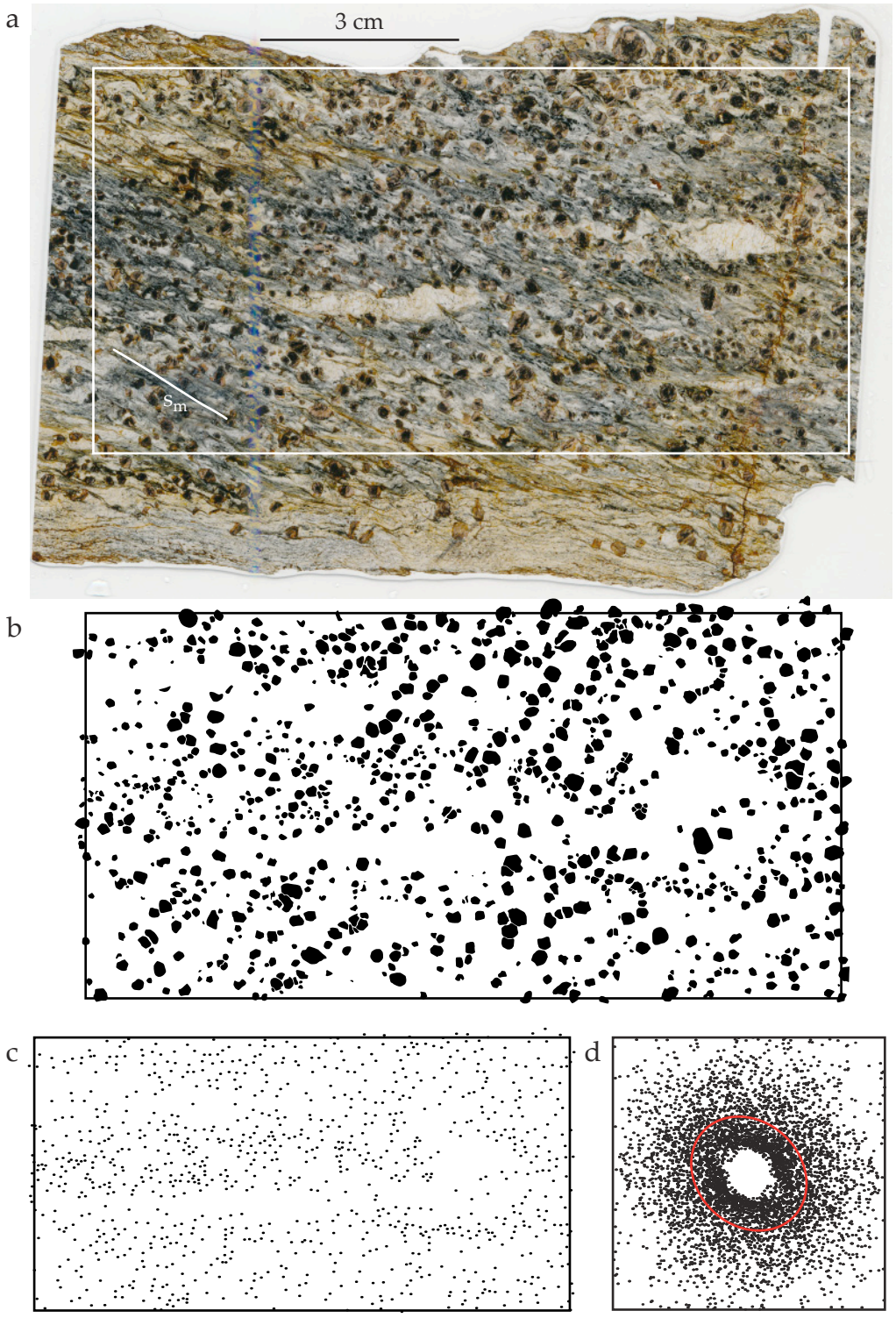

Figure 17: (a) Scanned thin section of sample 15c. The rectangle indicates the study area within the thin section. Orientation of the main foliation s_m is shown. (b) Redrawn garnet grains. (c) Location of centroids of the studied grains. (d) Fry plot calculated applying the delaunay triangulation nearest neighbour method (Mulchrone, 2003). Ellipticity of fitted ellipse is given by $R = 1.2$.

10.2 QUANTIFYING VOLUME STRAIN BASED ON VOLUME TRANSFER

Dissolution precipitation creep accommodates a large amount of deformation as can be inferred from the microstructural record. Therefore, quantifying the strain by dissolution precipitation is intriguing. Here I present a method to asses the volume transfer and related strain by dissolution precipitation in a two-dimensional approach. Following prerequisites have to be considered. First, in a two-dimensional section through a three-dimensional body, the area fraction of a phase equals approximately its volume fraction:

$$\frac{A_i}{A_{tot}} \approx \frac{V_i}{V_{tot}} \tag{11}$$

where A_i is area of phase i, A_{tot} the total area of the section, V_i the Volume of phase i and V_{tot} the total volume (Heilbronner and Barrett, 2014). It is consequently feasible to use thin sections to investigate the volumetric strain. Secondly, no change in volume is allowed because it would cause an underestimation of strain. A closed system where no dissolved material is transported far from the site of dissolution can be assumed for the here studied samples, i.e. no migration of the fluid out of the system occurred. This is indicated by the similarity of whole rock analyses for all samples and, especially, by nearly identical mineral compositions across the samples and microstructural domains (Fig. 9). For instance, the compositional variation for white mica in dissolution domains is identical with precipitation domains. This portends that the fluid phase is in local equilibrium. The volume can therefore be considered as constant during deformation. Internal inclusion fabrics in garnet reveal that strain caps and strain shadows were not developed prior to DPC-related deformation (Figs. 4, 5). The area of any section at this stage is given by:

$$A = P + M \tag{12}$$

where A is the total area, P the area of porphyroblasts and M the area of the matrix. After deformation by dissolution precipitation, matrix segregated to residual cleavage domains and sites of precipitation, mainly strain shadows. The area of a section after deformation is given by:

$$A = P + CD + SS \tag{13}$$

where CD is the area of CD domains and SS is the area of SS domains. This process can be schematically simplified (Fig. 18b). Pre-deformational, a unit square can thus be defined:

$$1 = P + M \tag{14}$$

After deformation, following statement is true:

$$1 = P + CD + SS \tag{15}$$

where CD is given by:

$$CD = a - P \tag{16}$$

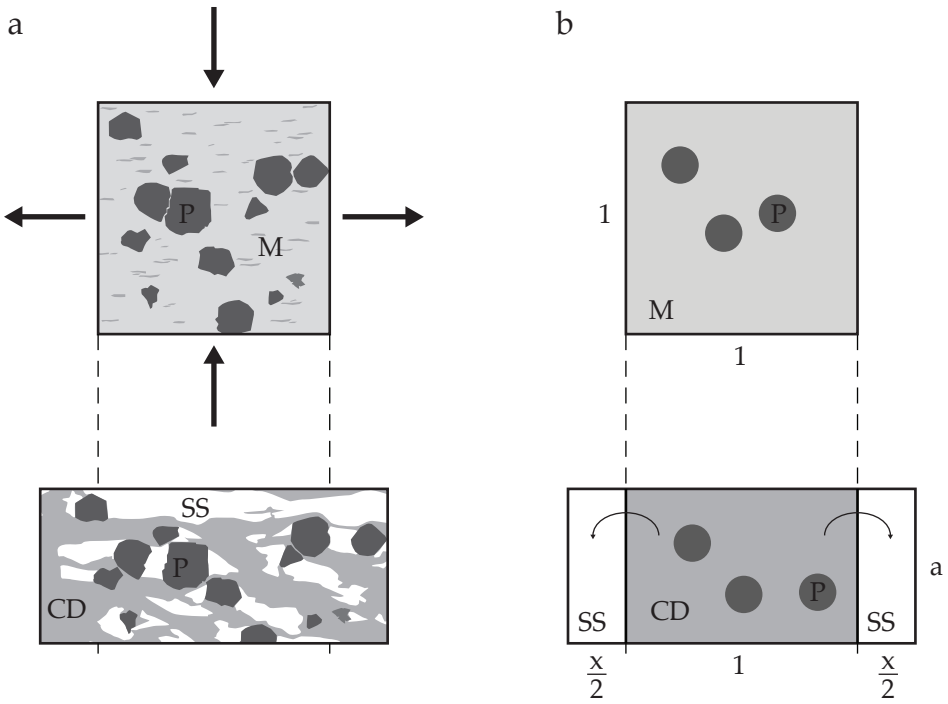

Figure 18: Schematic visualisation of the deformation accommodated by DPC. (a) Pre-deformational configuration of porphyroblasts in a matrix that exhibits a weak to spaced foliation (upper image). After defomation, the matrix separated to CD and SS domains (lower image). Note that pophyroblasts separated and diverged parallel to the stetching direction and converged parallel to the shortening direction. (b) Schematic sketch mimicking the processes that occurred in a. Upper image: initial setup of porphyroblasts and matrix in a unit square. Lower image: post-deformational configuration indicating the migration of material (precipitaion sites SS).

where a is the length of the shortened side of the rectangle; and S is given by:

$$SS = ax \tag{17}$$

where x the long side of the rectangle minus 1. The stretch s is defined as:

$$s = 1 + x \tag{18}$$

Substituting equation 17 into equation 18 gives:

$$s = 1 + \frac{SS}{a} \tag{19}$$

Rearranging the equations 15 and 16 and substituting them into equation 19 yields:

$$s = 1 + \frac{1 - P - CD}{CD + P} \tag{20}$$

$$s = \frac{1}{CD + P} \tag{21}$$

Eventually, substituting equation 15 into equation 21 makes the equation insensitive to the size of the investigated area:

$$s = \frac{P + SS + CD}{CD + P} \tag{22}$$

This method was applied to sample 10a2. Automatic outlining of the different domains is not possible because mineral detection in the scan is not unequivocal. Therefore, cross-checking with optical microscopy was inevitable. Using pixel counting, the respective areas were detected and applied in equation 22. A finite stretch of $s = 1.35$ was yielded for sample 10a3. However, some restrictions of this method are given by the uncertainty in differentiation between the sites of precipitation. The presence of many porphyroblasts renders the detection of the majority of precipitation sites admittedly easy. Yet, the microstructure is not everywhere that simple, which is why it was occasionally not possible to identify every spot of precipitated minerals. Reasons for this include that the sites of precipitation are too small (e.g. saddle reef structures in microfold hinges), the segregation of the matrix is not fully developed or dissolution and precipitation sites interweave on a very small scale. The calculation of strain is, therefore, rather underestimating the amount of deformation which was accommodated by dissolution precipitation creep.

10.3 QUANTIFYING VOLUME STRAIN IN CLEAVAGE DOMAINS BASED ON MASS TRANSFER

If the initial concentration of a less soluble phase in a volume of rock is known, the present-day concentration can be used to estimate the 'volume loss' or volumetric strain that occurred to achieve the present distribution of phases (Philpotts and Ague, 2009). Elements that are considered as only slightly mobile are, among others, Zr and Ti. For the studied samples, the Ti-bearing phases rutile and ilmenite appear enriched in cleavage domains and were therefore used to estimate

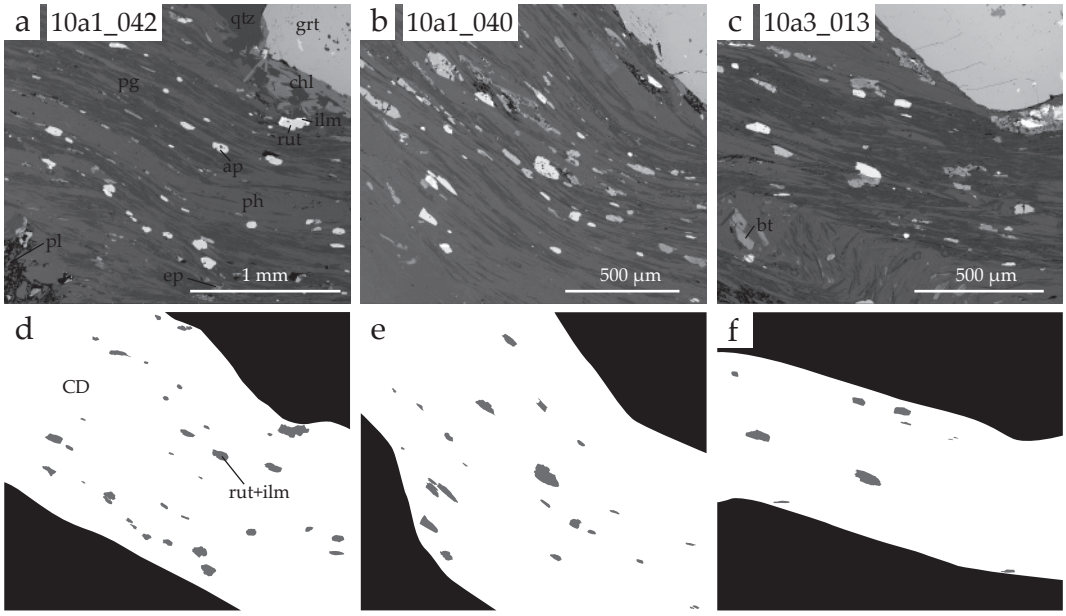

Figure 19: Selected sites where volumetric strain was estimated using mass balance. Image labels in upper left corners. (a-c) BSE images of CD domains. Labels indicate the sites on the thin section where the image was captured. (e-f) Digitised cleavage domains with traced Ti-bearing phases rutile and ilmenite.

the volumetric strain e of cleavage domains. Uniform distribution at initial stage is assumed. The calculations were done using the formula:

$$e = \left(\frac{c^0_{rut+ilm}}{c'_{rut+ilm}} \right) - 1 \tag{23}$$

where $c^0_{rut+ilm}$ is the initial concentration of Ti-bearing in the sample and $c'_{rut+ilm}$ is the concentration of Ti-bearing phases after mass transfer has occurred. Equation 23 is taken from Philpotts and Ague (2009) to where the reader is referred for the complete derivation of this formula (Philpotts and Ague, 2009, pp. 552). The initial concentration of Ti-bearing phases was modelled using THERIAK (de-Capitani and Petrakakis, 2010). For $550 - 600°C$ and $0.9 - 1.0$ GPa, rutile is the only stable Ti-bearing phase. Concentrations do not change significantly and vary between $c_{rut} \sim 0.57 - 0.59$ vol-% for different PT conditions. Thus, the available amount of rutile appears to be the determining parameter for c_{rut}, rather than the PT conditions. At the present state, rutile grains often exhibit rims of ilmenite. Therefore, Ti-bearing phases in the cleavage domains are defined as the sum of the area fractions of rutile plus ilmenite and approximate the volume fraction (see eq. 11). Image analysis was performed as described in the Methods chapter. The obtained values for volumetric strain via mass transfer in cleavage domains vary between $-0.75 < e < -0.60$ (Tab. 4).

10.4 QUANTIFYING STRAIN LOCALISATION BETWEEN GARNETS

Deformed and condensed strain caps indicate strain localisation between converging garnets. The length change can be easily measured where the initial length

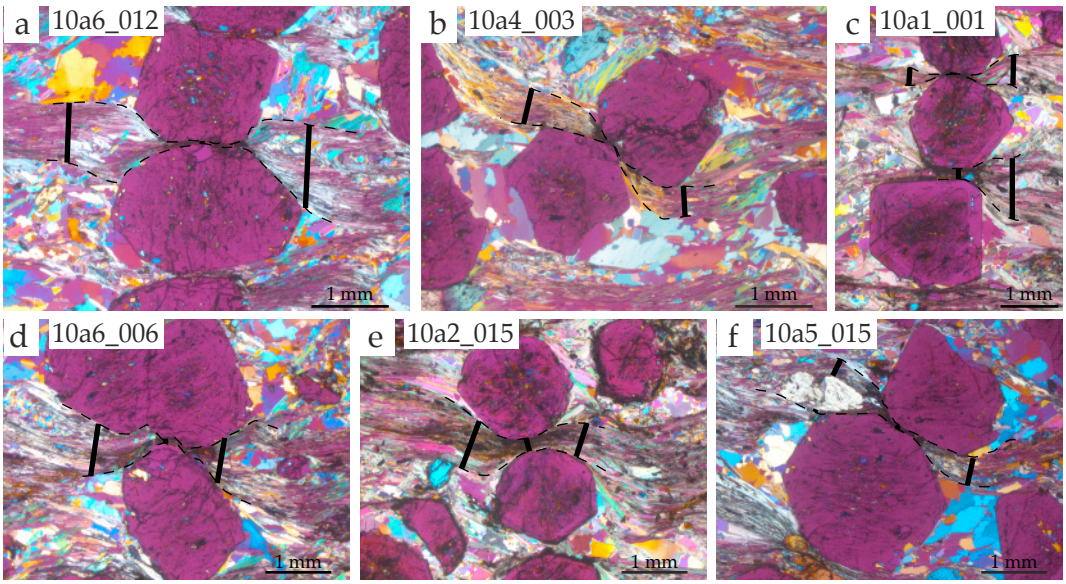

Figure 20: (a-f) Optical micrographs (crossed polarisers, compensatory red I inserted) showing selected sites where strain localises as a response to garnet convergence was quantified. Image labels in upper left corners.

of a cleavage domain is delivered in the microstructure (Fig. 20). The stretch s calculates:

$$s = \frac{l}{l_0} \tag{24}$$

where l_0 is the length before deformation and l is the length after deformation. 26 sites have been studied. Values yielded for stretch vary between $0.02 < s < 0.38$, the mean stretch is 0.15 (Tab. 4, for complete data set please refer to the appendix v).

10.5 DISCUSSION OF THE STRAIN ESTIMATES

The quantities for strain that are calculated above are not directly comparable. Strain was quantified as stretch s for the application of derivatives of Fry's method (see section 10.1), for the volume transfer by dissolution precipitation creep (see section 10.2) as well as for the matrix shortening associated with garnet convergence (see section 10.4). Whereas for mass balance, the strain was quantified as volumetric strain e (see section 10.3). e is also referred to as elongation and calculates:

$$e = s - 1 \tag{25}$$

When comparing positive and negative length (or volume) change, using stretch and elongation is inconvenient. This is demonstrated in a simple example: when a line is stretched to twice its length, $s = 2$ and $e = 1$, whereas when it is shortened to half its length, $s = 0.5$ and $e = 0.5$ (Means, 1976). The logarithmic strain,

$$\varepsilon = \ln(s) \tag{26}$$

strain	method/value	sample	s	e	ε
bulk	DTNNM	15d	1,20	0,20	0,18
	FryJ	15d	1,26	0,26	0,23
	volume transfer	10a2	1,35	0,35	0,30
CD	mass balance	10a1_036	0,31	−0,69	−1,17
	mass balance	10a1_042	0,25	−0,75	−1,39
	mass balance	10a3_013	0,42	−0,58	−0,87
convergence	max	10a4_003	0,02	−0,98	−4,10
	min	15c_003	0,38	−0,62	−0,97
	mean		0,15	−0,85	−2,17

Table 4: Translation to and comparison of the calculated strain values itemised per sample and method. For the bulk strain all results are shown. For localised strain in the matrix at convergence sites only selected results are presented.

constitutes a more intuitive quantity to characterise strain. For the example above, the respective stretching and shortening by a factor of 2 yields $\varepsilon = 0.69$ for stretching and $\varepsilon = -0.69$ for shortening These values are readily compared. Therefore the results from previous calculations were translated to logarithmic strain (Tab. 4).

The bulk strain which was obtained using a major part of a thin section yields similar results for the respective methods (Tab. 4). Bulk strain that was assessed using only the CD domains gave values that are significantly larger as compared to the methods mentioned before (Tab. 4). This discrepancy can be either explained by (i) the afore discussed underestimation of strain with the closed-system area-balance approach (section 10.2). There, the uncertainty whether precipitation sites are determined completely causes lower strain values. Or (ii), volume loss may have occurred. (iii), the strain in the CD domains is not representative for bulk strain. This is because the examined cleavage domains are sites where the characteristics of dissolution sites are very well developed. Therefore, these domains represent sites of higher amounts of dissolution than the bulk rock. This latter remark is supported by the observation of strikingly high enrichment of Ti-bearing phases in a dissolution seam between two garnets (Fig. 7e). There, the strain has been highly increased locally. All these causes are reasonable explanations for the discrepancy in strain estimates using different methods. Thus, an interplay of all three of these reasons is assumed. However, the localisation of strain in the matrix in convergence domains still distinctly exceeds the bulk strain. Garnets approach each other due to bulk deformation. Therefore, considering an external reference frame the strain can be assumed as approximately homogeneous. This in turn, means that on a small scale, particularly in between garnets, the space problem between converging garnets induces increased deformation. Highly enriched less mobile phases in these areas indicate that dissolution precipitation creep accommodates this local-

ised strain. Therefore it can be concluded that the interaction of garnets causes accelerated dissolution precipitation creep.

However, after the garnets came to close proximity, convergence does not cease. When the matrix is deformed to a certain width of a few tens of micrometers, garnets take up strain. As a consequence, garnets deform by fracturing and dissolution. The fact that garnets fracture suggests that the stress field inside the crystals is not homogeneous, contrary to the analytical models used for strong inclusions in viscous flow (Schmid and Podladchikov, 2003). This has already been shown numerically for the interaction of crystals in a melt (Deubelbeiss et al., 2011). There, in-series contacts develop so-called force chains parallel to the instantaneous shortening direction which is very similar to what could be observed in this study (6a, Fig. 4 in Deubelbeiss et al., 2011). Whether or not, during ongoing deformation, high differential stresses emerge between colliding clasts (which eventually would cause deviations from lithostatic pressure) can not be fully answered, however. On the one hand, metapelites from the Steinplan area tell us that there *must* have been heterogeneities in stress to fracture garnets. On the other hand, mineral compositions do not record local pressure variations. Plus, where high stresses would be expected, the finite strain is highly increased in the matrix *and* in the garnets. Therefore, garnets in a viscous, deforming matrix cannot be considered as rigid. At least not under high pressure-temperature conditions like in the here studied amphibolite-facies metapelites. Rather, they are strong, deformable inclusions which respond to strain by the different deformation mechanisms of fracturing and dissolution.

11

TIME, STRAIN RATE AND VISCOSITY

11.1 ESTIMATING TIME, STRAIN RATE AND VISCOSITY

Overgrowth of strain shadows and strain caps in the outermost rim of garnets proves that these rims started to grow at the DPC-dominated stage of deformation. The rim exhibits characteristics for diffusional increase of Mg and concomitant decrease in Fe-content (Fig. 11, Tab. 2). Diffusion is recognisable in bell-shaped increase/decrease around cracks in inner parts of garnet (Fig. 12) and gradual alteration towards the rim (Fig. 11). The lower bound for diffusion can be set after the onset of the main deformation because the altered zone developed in the outermost rim. In sample 07g, this Mg-enriched, Fe-depleted rim is truncated as a result of garnet dissolution at a site of convergence in sample 07g (Fig. 12). The erosion of the diffusion rim sets the upper bound of diffusion before the end of the main deformation. This well defined constraint of the stage at which diffusion occurred makes it feasible to calculate the timing of deformation with the help of diffusion. The characteristic diffusion length L is given by:

$$L = 2\sqrt{Dt} \tag{27}$$

where D is the diffusion coefficient and t is time. Because the alteration within the diffusional rims only affects Mg and Fe it is sufficient to calculate solely the Mg diffusion, because the diffusion can be described as $Fe + Mg = 1$. The diffusion coefficient in dependance of pressure and temperature for Mg in garnet is given by:

$$D(P,T) = D_0 \exp\left(-\frac{Q + (P-1)\Delta V}{RT}\right) \tag{28}$$

where D_0 is the pre-exponential factor, Q is the activation energy at 1 bar, ΔV is the activation volume and R is the gas constant (Ganguly et al., 1998). The diffusion coefficient is calculated based on experimental data of pyrope-almandine diffusion couples (Ganguly et al., 1998). For 0.9 GPa, the diffusion coefficients are given in table 5. Rearranging equation 27 yields:

$$t = \frac{L^2}{4D} \tag{29}$$

Applying equation 29, the time for diffusion is readily computed (Tab. 5). The mean duration of diffusion at garnet rims is calculated with 759 myr at 575°C and 98 myr at 625°C, rendering how temperature-sensitive diffusion and hence the obtained time estimates are. The length and duration of diffusion around cracks in the interior of garnet are much shorter. This is due to hampered diffusion along the cracks in comparison to the rims of garnet which are in direct contact with the fluid phase at the garnet-matrix interface. Therefore, only the diffusion at garnet rims are considered for application to the simple diffusion

	number	L [µm]	t [myr]		
			575°C	600°C	625°C
D_{Mg}			$5.07 \cdot 10^{-25}$	$1.24 \cdot 10^{-24}$	$3.93 \cdot 10^{-24}$
rim	10a1_001	200	625.40	218.30	80.79
		280	1225.80	427.86	158.35
	10a1_007	172	462.60	161.45	59.75
	10a1_016	158	390.30	136.24	50.42
	10a1_021	212	702.70	245.28	90.77
		272	1156.80	403.76	149.43
	10a2 002	219	749.90	261.74	96.87
mean			759.07	264.95	98.05
crack	10a1_021	59	54.40	19.00	7.03
		49	37.50	13.10	4.85
		39	23.80	8.30	3.07
		64	64.00	22.35	8.27
	10a1_027	33	17.00	5.94	2.20
	10a2_003	23	8.30	2.89	1.07
		38	22.60	7.88	2.92
		33	17.00	5.94	2.20
mean			30.58	10.68	3.95

Table 5: Extended table 2 with added estimation for the time of diffusion.

model of equation 27. However, the obtained values for the timing of diffusion appear very unrealistic in consideration of the geodynamic model for the metamorphic evolution of the Koralpe-Wölz nappe system (Schuster et al., 2004). Sm-Nd isotopic ages of garnet and Rb-Sr isotopic ages of phengite constrain the peak metamorphism close to 90 Ma for the internal parts of the Koralpe-Wölz nappe system which are the eclogites of the Koralpe and Saualpe area (Thöni and Jagoutz, 1993). Cooling of the Koralpe-Wölz nappes below 300°C (A-Ar, K-Ar and Rb-Sr mica ages) appeared between $90 - 85$ Ma in the northern parts and around 70 Ma in the southern parts of the nappe system (Thöni and Jagoutz, 1993; Schuster et al., 2004). This timeframe of circa 20 myr has to include the high-temperature deformation of the garnet mica schist investigated in this study. Therefore, the time steps of 5, 10 and 15 myr were assumed for the length of DPC-dominated deformation in order to roughly estimate the order of the strain rate. The strain rate $\dot{\varepsilon}$ was calculated for the bulk rock, cleavage domains and for the sites of enhanced dissolution between porphyroblasts, respectively (Tabs. 6, 7). The order of magnitude stays about the same for 5, 10 and 15 myr. For 5 myr, the mean strain rate of the bulk rock is $8.06 \cdot 10^{-15}\, s^{-1}$. The mean strain rate of the cleavage domains $2.03 \cdot 10^{-14}\, s^{-1}$, which is 2.5 times higher than the strain rate rate of the bulk rock.

Quartz microfabrics which are preserved in garnet display conditions of static recrystallisation during the main deformation. This indicates that low differential stresses were predominant at this stage. Similar features were described by Stöckhert et al. (1997) who inferred maximum differential stresses of 2 MPa at $600°C$ from experimental flow laws for quartz. For the here studied samples, $600°C$ were determined for the metamorphic conditions at which the deformation occurred. Therefore, 2 MPa can be assumed as maximum differential stress for the stage of deformation at which strain caps and shadows developed. When strain rate and stress are known, the viscosity η can be calculated according to the equation:

$$\eta = \frac{\sigma}{2\dot{\varepsilon}} \tag{30}$$

where σ is the maximum differential stress. The viscosity is given for the bulk and CD domains only because a change of viscosity cannot be expected in convergence areas (Tabs. 6, 7).

Knowing the viscosity of the cleavage domains as well as the strain rate between garnets, equation 30 can be used to calculate the stress in between garnets. Rearranging equation 30 yields:

$$\sigma = 2\dot{\varepsilon}\eta \tag{31}$$

Values for the maximum differential stress in convergence areas lie between 1.72 MPa and can be as high as 32.67 MPa, the mean is 4.36 MPa. Whether or nor the calculated stress was reached between the garnets is not evident in the samples. What can be inferred from the microstructural record however, is that strain is highly localised between porphyroblasts. This deformation was accommodated by increased dissolution of white mica which suggests that higher stresses between porphyroblasts enhance dissolution precipitation creep in domains of convergence in the here studied rocks.

	s	'positive' s	$\dot{\varepsilon}$ $[s^{-1}]$	η[Pa·s]	σ[MPa]
time			5 *myr*		
bulk	1.20	1.20	$7.62 \cdot 10^{-15}$	$1.31 \cdot 10^{20}$	
	1.26	1.26	$8.00 \cdot 10^{-15}$	$1.25 \cdot 10^{20}$	
	1.35	1.35	$8.57 \cdot 10^{-15}$	$1.17 \cdot 10^{20}$	
CD	0.31	3.23	$2.05 \cdot 10^{-14}$	$4.88 \cdot 10^{19}$	
	0.25	4.00	$2.54 \cdot 10^{-14}$	$3.94 \cdot 10^{19}$	
	0.42	2.38	$1.51 \cdot 10^{-14}$	$6.62 \cdot 10^{19}$	
convergence - max	0.02	50.00	$3.17 \cdot 10^{-13}$		32.67
convergence - min	0.38	2.63	$1.67 \cdot 10^{-14}$		1.72
convergence - mean	0.15	6.67	$4.23 \cdot 10^{-14}$		4.36
			mean	*mean*	
		bulk	$8.06 \cdot 10^{-15}$	$1.24 \cdot 10^{20}$	
		CD	$2.03 \cdot 10^{-14}$	$5.15 \cdot 10^{19}$	
time			10 *myr*		
bulk	1.20	1.20	$3.16 \cdot 10^{-15}$	$2.63 \cdot 10^{20}$	
	1.26	1.26	$4.00 \cdot 10^{-15}$	$2.50 \cdot 10^{20}$	
	1.35	1.35	$4.29 \cdot 10^{-15}$	$2.33 \cdot 10^{20}$	
CD	0.31	3.23	$1.02 \cdot 10^{-14}$	$9.77 \cdot 10^{19}$	
	0.25	4.00	$1.27 \cdot 10^{-14}$	$7.88 \cdot 10^{19}$	
	0.42	2.38	$7.56 \cdot 10^{-15}$	$1.32 \cdot 10^{20}$	
convergence - max	0.02	50.00	$1.59 \cdot 10^{-13}$		32.67
convergence - min	0.38	2.63	$8.35 \cdot 10^{-15}$		1.72
convergence - mean	0.15	6.67	$2.12 \cdot 10^{-14}$		4.36
			mean	*mean*	
		bulk	$4.03 \cdot 10^{-15}$	$2.49 \cdot 10^{20}$	
		CD	$1.02 \cdot 10^{-14}$	$1.03 \cdot 10^{20}$	

Table 6: Strain rate, viscosity and stress between converging garnets for 5 and 10 myr of deformation. The values of stretch are taken from table 4. For shortening stretch of the strain analyses of CD domains and convergence between garnets, the inverse, 'positive' stretch was calculated. The strain rate $\dot{\varepsilon}$ is given for all microstructural domains. The viscosity η is given for the bulk and CD domains. Calculations of maximum differential stress σ for convergence zones between garnets.

	s	'positive' s	$\dot{\varepsilon}\,[s^{-1}]$	η[Pa·s]	σ[MPa]
time			15 *myr*		
bulk	1.20	1.20	$2.54 \cdot 10^{-15}$	$3.94 \cdot 10^{20}$	
	1.26	1.26	$2.67 \cdot 10^{-15}$	$3.75 \cdot 10^{20}$	
	1.35	1.35	$2.86 \cdot 10^{-15}$	$3.50 \cdot 10^{20}$	
CD	0.31	3.23	$6.83 \cdot 10^{-15}$	$1.46 \cdot 10^{20}$	
	0.25	4.00	$8.47 \cdot 10^{-15}$	$1.18 \cdot 10^{20}$	
	0.42	2.38	$5.04 \cdot 10^{-15}$	$1.98 \cdot 10^{20}$	
convergence - max	0.02	50.00	$1.03 \cdot 10^{-13}$		32.67
convergence - min	0.38	2.63	$5.57 \cdot 10^{-15}$		1.72
convergence - mean	0.15	6.67	$1.41 \cdot 10^{-14}$		4.36
			mean	*mean*	
		bulk	$2.69 \cdot 10^{-15}$	$3.73 \cdot 10^{20}$	
		CD	$6.78 \cdot 10^{-15}$	$1.54 \cdot 10^{20}$	

Table 7: Strain rate, viscosity and stress between converging garnets for 15 myr of deformation. The values of stretch are taken from table 4. For shortening stretch of the strain analyses of CD domains and convergence between garnets, the inverse, 'positive' stretch was calculated. The strain rate $\dot{\varepsilon}$ is given for all microstructural domains. The viscosity η is given for the bulk and CD domains. Calculations of maximum differential stress σ for convergence zones between garnets.

Part IV

CONCLUSION

12 CONCLUSION

The here presented study illuminates in a different complexion how vital the presence of porphyroblasts in deforming rocks is. Like in many other studies, the internal fabric and chemical variations in garnets were successfully utilised to reconstruct the metamorphic and deformation history of porphyroblastic mica schists from the Wölz unit. However, and this is peculiar about the in hand study, the dense population of garnets caused the matrix to separate during deformation by dissolution precipitation creep. The matrix differentiated to dissolution sites and precipitation sites in the respective quadrants of stretching and shortening around the crystals. The distinct separation of sinks and sources was used to quantify the bulk strain which was accommodated by dissolution precipitation creep and revealed a stretch of $s = 1.35$. This shows that dissolution precipitation creep is a very effective deformation mechanism for high-grade metapelites. This is an important finding because it applies to a type of rock which is globally common in collisional orogens.

When porphyroblasts start to interact during ongoing deformation they cause localisation of strain in their interstices. This in turn leads to an accelerated strain rate and probably stresses in these domains. When garnets come to close vicinity they do not stop to converge. Instead, garnets deform through fracturing and dissolution. Therefore, porphyroblasts cannot be considered as rigid inclusions in the investigated rocks, contrary to the setup of many analogue and numerical models. The here studied samples show that particle deformation occurs in a weaker, deforming matrix. Plastic deformation of strong particles in viscous flow can cause the bulk rheology to change as has been shown previously (Deubelbeiss et al., 2011; Yamato et al., 2012). Hence, particle deformation needs to be implemented when modelling inclusion-marix systems.

Phengite is present in dissolution as well as precipitation sites which are potential areas where stress-induced deviations in lithostatic pressure could occur. Although phengite is a common geobarometer, it does not record any variations in pressure between specific microstructural domains of convergence and dilation. Either rapid equilibration by the ubiquitous fluid phase or slow adaption of the composition (Massonne and Schreyer, 1987) to changes in PT condition render possible explanations. However, phengite constitutes an impractical tool for answering this question. Therefrom it can be inferred that even if deviations in lithostatic pressure occur as a consequence of deformation in between porphyroblasts, their evidence might not be recorded in the geological record.

BIBLIOGRAPHY

Abu-Alam, T., Stüwe, K., 2011. Polyphase strain caps. Mineralogy and Petrology 101 (1), 1–19. (Cited on page 21.)

Ague, J., Carlson, W., 2013. Metamorphism as garnet sees it: The kinetics of nucleation and growth, equilibration, and diffusional relaxation. Elements 9 (6), 439–445. (Cited on page 3.)

Arbaret, L., Diot, H., Bouchez, J.-L., 1996. Shape fabrics of particles in low concentration suspensions: 2D analogue experiments and application to tiling in magma. Journal of Structural Geology 18 (7), 941–950. (Cited on page 3.)

Baldwin, J. A., Powell, R., Brown, M., Moraes, R., Fuck, R. A., Sep. 2005. Modelling of mineral equilibria in ultrahigh-temperature metamorphic rocks from the Anápolis–Itauçu Complex, central Brazil. Journal of Metamorphic Geology 23 (7), 511–531.
URL http://onlinelibrary.wiley.com/doi/10.1111/j.1525-1314.2005.00591.x/abstract (Cited on page 43.)

Baxter, E., Caddick, M., Ague, J., 2013. Garnet: Common mineral, uncommonly useful. Elements 9 (6), 415–419. (Cited on page 3.)

Bestel, M., Gawronski, T., Abart, R., Rhede, D., 2009. Compositional zoning of garnet porphyroblasts from the polymetamorphic Wölz Complex, Eastern Alps. Mineralogy and Petrology 97 (3-4), 173–188. (Cited on pages 3, 4, and 5.)

Caddick, M., Kohn, M., 2013. Garnet: Witness to the evolution of destructive plate boundaries. Elements 9 (6), 427–432. (Cited on page 3.)

Clark, P. J., Evans, F. C., Oct. 1954. Distance to nearest neighbor as a measure of spatial relationships in populations. Ecology 35 (4), 445.
URL http://www.esajournals.org/doi/abs/10.2307/1931034 (Cited on page 35.)

Coggon, R., Holland, T. J. B., Sep. 2002. Mixing properties of phengitic micas and revised garnet-phengite thermobarometers. Journal of Metamorphic Geology 20 (7), 683–696.
URL http://onlinelibrary.wiley.com/doi/10.1046/j.1525-1314.2002.00395.x/abstract (Cited on page 43.)

Connolly, J., Thompson, A., 1989. Fluid and enthalpy production during regional metamorphism. Contributions to Mineralogy and Petrology 102 (3), 347–366. (Cited on page 39.)

Crespi, J., 1986. Some guidelines for the practical application of Fry's method of strain analysis. Journal of Structural Geology 8 (7), 799–808. (Cited on page 50.)

deCapitani, C., Petrakakis, K., 2010. The computation of equilibrium assemblage diagrams with Theriak/Domino software. American Mineralogist 95 (7), 1006–1016. (Cited on pages 43 and 55.)

deCapitani, C., Petrakakis, K., 2012. THERIAK-DOMINO.
URL http://titan.minpet.unibas.ch/minpet/theriak/theruser.html
(Cited on page 43.)

Dell'Angelo, L., Tullis, J., 1996. Textural and mechanical evolution with progressive strain in experimentally deformed aplite. Tectonophysics 256 (1-4 SPEC. ISS.), 57–82. (Cited on page 3.)

Deubelbeiss, Y., Kaus, B., Connolly, J., Caricchi, L., 2011. Potential causes for the non-Newtonian rheology of crystal-bearing magmas. Geochemistry, Geophysics, Geosystems 12 (5). (Cited on pages 3, 4, 58, and 67.)

Doube, M., Kłosowski, M. M., Arganda-Carreras, I., Cordelières, F. P., Dougherty, R. P., Jackson, J. S., Schmid, B., Hutchinson, J. R., Shefelbine, S. J., Dec. 2010. BoneJ: free and extensible bone image analysis in ImageJ. Bone 47 (6), 1076–1079.
URL http://linkinghub.elsevier.com/retrieve/pii/S8756328210014419
(Cited on page 36.)

Dougherty, R., Kunzelmann, K.-H., Aug. 2007. Computing Local Thickness of 3D Structures with ImageJ. Microscopy and Microanalysis 13 (S02).
URL http://journals.cambridge.org/action/displayFulltext?type=1&fid=1212988&jid=MAM&volumeId=13&issueId=S02&aid=1212984&bodyId=&membershipNumber=&societyETOCSession= (Cited on page 36.)

Drury, M., Urai, J., 1990. Deformation-related recrystallization processes. Tectonophysics 172 (3-4), 235–253. (Cited on page 16.)

Erslev, E., 1988. Normalized center-to-center strain analysis of packed aggregates. Journal of Structural Geology 10 (2), 201–209. (Cited on page 50.)

Erslev, E., Ge, H., 1990. Least-squares center-to-center and mean object ellipse fabric analysis. Journal of Structural Geology 12 (8), 1047–1059. (Cited on pages 49 and 50.)

Faryad, S., Hoinkes, G., 2003. P-T gradient of Eo-Alpine metamorphism within the Austroalpine basement units east of the Tauern Window (Austria). Mineralogy and Petrology 77 (1-2), 129–159. (Cited on page 5.)

Ferreira, T., Rasband, W. S., 2010. ImageJ User Guide — IJ 1.46.
URL imagej.nih.gov/ij/docs/guide/ (Cited on page 50.)

Frisch, W., Vavra, G., Winkler, M., 1993. Evolution of the Penninic basement of the Eastern Alps. In: Raumer, F. J., Neubauer, F. (Eds.), Pre-Mesozoic geology in the Alps, 1st Edition. Springer, Heidelberg, pp. 349–360. (Cited on page 5.)

Froitzheim, N., Schmid, S., Frey, M., 1996. Mesozoic paleogeography and the timing of eclogitefacies metamorphism in the Alps: A working hypothesis. Eclogae Geologicae Helvetiae 89 (1), 81–110. (Cited on page 5.)

Fry, N., 1979. Random point distributions and strain measurement in rocks. Tectonophysics 60 (1-2), 89–105. (Cited on page 49.)

Gaidies, F., Abart, R., De Capitani, C., Schuster, R., Connolly, J., Reusser, E., 2006. Characterization of polymetamorphism in the Austroalpine basement east of the Tauern Window using garnet isopleth thermobarometry. Journal of Metamorphic Geology 24 (6), 451–475. (Cited on pages 3 and 4.)

Gaidies, F., Capitani, C., Abart, R., Schuster, R., 2008. Prograde garnet growth along complex P-T-t paths: Results from numerical experiments on polyphase garnet from the Wölz Complex (Austroalpine basement). Contributions to Mineralogy and Petrology 155 (6), 673–688. (Cited on page 5.)

Ganguly, J., Cheng, W., Chakraborty, S., 1998. Cation diffusion in aluminosilicate garnets: Experimental determination in pyrope-almandine diffusion couples. Contributions to Mineralogy and Petrology 131 (2), 171–180. (Cited on page 59.)

Gratier, J.-P., Dysthe, D., Renard, F., 2013. The Role of Pressure Solution Creep in the Ductility of the Earth's Upper Crust. Vol. 54. (Cited on pages 12, 21, 39, and 41.)

Greene, G., Kristiansen, K., Meyer, E., Boles, J., Israelachvili, J., 2009. Role of electrochemical reactions in pressure solution. Geochimica et Cosmochimica Acta 73 (10), 2862–2874. (Cited on page 41.)

Groome, W., Johnson, S., Koons, P., 2006. The effects of porphyroblast growth on the effective viscosity of metapelitic rocks: Implications for the strength of the middle crust. Journal of Metamorphic Geology 24 (5), 389–407. (Cited on page 3.)

Habler, G., Thöni, M., 2001. Preservation of Permo-Triassic low-pressure assemblages in the Cretaceous high-pressure metamorphic Saualpe crystalline basement (Eastern Alps, Austria). Journal of Metamorphic Geology 19 (6), 679–697. (Cited on page 5.)

Hawkins, A., Selverstone, J., Brearley, A., Beane, R., Ketcham, R., Carlson, W., 2007. Origin and mechanical significance of honeycomb garnet in high-pressure metasedimentary rocks from the Tauern Window, Eastern Alps. Journal of Metamorphic Geology 25 (5), 565–583. (Cited on pages 16 and 18.)

Heilbronner, R., Barrett, S. D., 2014. Image analysis in earth sciences microstructures and textures of earth materials. Springer, Heidelberg. (Cited on pages 34, 35, and 52.)

Holland, T., Powell, R., 1998. An internally consistent thermodynamic data set for phases of petrological interest. Journal of Metamorphic Geology 16 (3), 309–343. (Cited on page 43.)

Ildefonse, B., Sokoutis, D., Mancktelow, N., 1992. Mechanical interactions between rigid particles in a deforming ductile matrix. Analogue experiments in simple shear flow. Journal of Structural Geology 14 (10), 1253–1266. (Cited on page 3.)

Jerram, D., Cheadle, M., Hunter, R., Elliott, M., 1996. The spatial distribution of grains and crystals in rocks. Contributions to Mineralogy and Petrology 125 (1), 60–74. (Cited on pages xi, 35, and 37.)

Jessell, M., Bons, P., Griera, A., Evans, L., Wilson, C., 2009. A tale of two viscosities. (Cited on page 3.)

Johnson, S., 1999. Porphyroblast microstructures: A review of current and future trends. American Mineralogist 84 (11-12), 1711–1726. (Cited on page 3.)

Johnson, S., Lenferink, H., Marsh, J., Price, N., Koons, P., West Jr., D., 2009. Kinematic vorticity analysis and evolving strength of mylonitic shear zones: New data and numerical results. Geology 37 (12), 1075–1078. (Cited on page 3.)

Johnson, S. E., Bell, T. H., Jan. 1996. How useful are 'millipede' and other similar porphyroblast microstructures for determining synmetamorphic deformation histories? Journal of Metamorphic Geology 14 (1), 15–28.
URL http://onlinelibrary.wiley.com/doi/10.1111/j.1525-1314.1996.00015.x/abstract (Cited on page 17.)

Kretz, R., Aug. 2006. Shape, size, spatial distribution and composition of garnet crystals in highly deformed gneiss of the otter lake area, quebec, and a model for garnet crystallization. Journal of Metamorphic Geology 24 (6), 431–449.
URL http://doi.wiley.com/10.1111/j.1525-1314.2006.00647.x (Cited on pages xi, 33, 35, and 36.)

Lexa, O., Feb. 2014. PolyLX - the MATLAB™ toolbox for quantitative analysis of microstructures.
URL http://petrol.natur.cuni.cz/~ondro/polylx:home (Cited on page 50.)

Mancktelow, N., 2008. Tectonic pressure: Theoretical concepts and modelled examples. Lithos 103 (1-2), 149–177. (Cited on page 41.)

Mancktelow, N., 2013. Behaviour of an isolated rimmed elliptical inclusion in 2D slow incompressible viscous flow. Journal of Structural Geology 46, 235–254. (Cited on page 3.)

Marmo, B., Clarke, G., Powell, R., 2002. Fractionation of bulk rock composition due to porphyroblast growth: Effects on eclogite facies mineral equilibria, Pam Peninsula, New Caledonia. Journal of Metamorphic Geology 20 (1), 151–165. (Cited on page 43.)

Marques, F., Mandal, N., Taborda, R., Antunes, J., Bose, S., 2014. The behaviour of deformable and non-deformable inclusions in viscous flow. Earth-Science Reviews 134, 16–69. (Cited on page 3.)

Massonne, H.-J., Schreyer, W., 1987. Phengite geobarometry based on the limiting assemblage with K-feldspar, phlogopite, and quartz. Contributions to Mineralogy and Petrology 96 (2), 212–224. (Cited on pages 41, 42, and 67.)

Means, W. D., 1976. Stress and Strain - Basic Concepts of Continuum Mechanics for Geologists. Springer, New York. (Cited on page 56.)

Meschede, M., 1994. Methoden der Strukturgeologie: ein Leitfaden zur Aufnahme und Auswertung strukturgeologischer Daten im Gelände und im Labor. Enke, Stuttgart. (Cited on page 49.)

Mulchrone, K., 2003. Application of Delaunay triangulation to the nearest neighbour method of strain analysis. Journal of Structural Geology 25 (5), 689–702. (Cited on pages 49, 50, and 51.)

Passchier, C., Simpson, C., 1986. Porphyroclast systems as kinematic indicators. Journal of Structural Geology 8 (8), 831–843. (Cited on page 3.)

Passchier, C., Trouw, R., 2005. Microtectonics. (Cited on pages 3, 12, 14, and 17.)

Paterson, M. S., Luan, F. C., Jan. 1990. Quartzite rheology under geological conditions. Geological Society, London, Special Publications 54 (1), 299–307.
URL http://sp.lyellcollection.org/content/54/1/299 (Cited on page 39.)

Pennacchioni, G., Di Toro, G., Mancktelow, N., 2001. Strain-insensitive preferred orientation of porphyroclasts in Mont Mary mylonites. Journal of Structural Geology 23 (8), 1281–1298. (Cited on page 4.)

Petrakakis, K., Dietrich, H., 1985. MINSORT - A program for the processing and archivation of microprobe analyses of silicate and oxide minerals. Neues Jahrbuch für Mineralogie 8, 379–384. (Cited on page 7.)

Philpotts, A., Ague, J. J., Jan. 2009. Principles of Igneous and Metamorphic Petrology. Cambridge University Press. (Cited on pages 54 and 55.)

Piazolo, S., Bons, P., Passchier, C., 2002. The influence of matrix rheology and vorticity on fabric development of populations of rigid objects during plane strain deformation. Tectonophysics 351 (4), 315–329. (Cited on page 3.)

Ramsay, J., 1974. Development of Chevron Folds. Bulletin of the Geological Society of America 85 (11), 1741–1754. (Cited on page 14.)

Ramsay, J. G., Huber, M. I., 1983. The techniques of modern structural geology. Academic Press, London; New York. (Cited on pages 49 and 50.)

Rasband, W. S., 1997. ImageJ.
URL http://imagej.nih.gov/ij/ (Cited on page 7.)

Rice, A. H. N., Habler, G., Carrupt, E., Cotza, G., Wiesmayr, G., Schuster, R., Sölva, H., Thöni, M., Koller, F., 2006. Textural Sector-Zoning in Garnet: Theoretical Patterns and Natural Examples from Alpine Metamorphic Rocks. Austrian Journal of Earth Sciences 99, 70–89. (Cited on page 18.)

Rice, A. H. N., Mitchell, J., 1991. Porphyroblast textural sector-zoning and matrix displacement. Mineralogical Magazine 55 (380), 379–396.
URL http://www.minersoc.org/pages/Archive-MM/Volume_55/55-380-379.pdf (Cited on page 18.)

Schindelin, J., Arganda-Carreras, I., Frise, E., Kaynig, V., Longair, M., Pietzsch, T., Preibisch, S., Rueden, C., Saalfeld, S., Schmid, B., Tinevez, J.-Y., White, D. J., Hartenstein, V., Eliceiri, K., Tomancak, P., Cardona, A., Jun. 2012. Fiji: an open-source platform for biological-image analysis. Nature Methods 9 (7), 676–682.
URL http://www.nature.com/doifinder/10.1038/nmeth.2019 (Cited on page 7.)

Schmid, D. W., Podladchikov, Y. Y., Oct. 2003. Analytical solutions for deformable elliptical inclusions in general shear. Geophysical Journal International 155 (1), 269–288.
URL http://onlinelibrary.wiley.com/doi/10.1046/j.1365-246X.2003.02042.x/abstract (Cited on pages 3, 41, and 58.)

Schmid, S., Fügenschuh, B., Kissling, E., Schuster, R., 2004. Tectonic map and overall architecture of the Alpine orogen. Eclogae Geologicae Helvetiae 97 (1), 93–117. (Cited on pages 4 and 5.)

Schuster, R., Koller, F., Hoeck, V., Hoinkes, G., Bousquet, R., 2004. Explanatory notes to the map: Metamorphic structure of the Alps. Metamorphic evolution of the Eastern Alps. Mitteilungen der Österreichischen Mineralogischen Gesellschaft 149, 115–123. (Cited on pages 4, 5, and 61.)

Schuster, R., Thöni, M., 1996. Permian garnets: indication for a regional Permian metamorphism in the southern part of the Austroalpine basement units. Mitteilungen der Gesellschaft der Geologie- und Bergbaustudenten in Österreich 45, 111–141. (Cited on page 5.)

Spiess, R., Peruzzo, L., Prior, D., Wheeler, J., 2001. Development of garnet porphyroblasts by multiple nucleation,coalescence and boundary misorientation-driven rotations. Journal of Metamorphic Geology 19 (3), 269–290. (Cited on page 17.)

Stipp, M., Stünitz, H., Heilbronner, R., Schmid, S., 2002. The eastern Tonale fault zone: A 'natural laboratory' for crystal plastic deformation of quartz over a temperature range from 250 to 700 °C. Journal of Structural Geology 24 (12), 1861–1884. (Cited on pages 16, 17, and 40.)

Stöckhert, B., Massonne, H.-J., Nowlan, E., 1997. Low differential stress during high-pressure metamorphism: The microstructural record of a metapelite from the Eclogite Zone, Tauern Window, Eastern Alps. Lithos 41 (1-3), 103–118. (Cited on pages 3, 18, 39, and 61.)

Thöni, M., Jagoutz, E., 1993. Isotopic constraints for eo-Alpine high-P metamorphism in the Austroalpine nappes of the Eastern Alps: bearing on Alpine orogenesis. Schweizer Mineralogische und Petrographische Mitteilungen 73, 177–189. (Cited on pages 5 and 61.)

Waldron, J., Wallace, K., 2007. Objective fitting of ellipses in the centre-to-centre (Fry) method of strain analysis. Journal of Structural Geology 29 (9), 1430–1444. (Cited on pages 49 and 50.)

Wassmann, S., Stöckhert, B., 2013a. Low stress deformation of garnet by incongruent dissolution precipitation creep. Journal of Structural Geology 46, 200–219. (Cited on pages 21 and 41.)

Wassmann, S., Stöckhert, B., 2013b. Rheology of the plate interface - Dissolution precipitation creep in high pressure metamorphic rocks. Tectonophysics 608, 1–29. (Cited on pages 12 and 21.)

Wheeler, J., 1992. Importance of pressure solution and coble creep in the deformation of polymineralic rocks. Journal of Geophysical Research 97 (B4), 4579–4586. (Cited on page 41.)

White, R. W., Powell, R., Holland, T. J. B., Jun. 2007. Progress relating to calculation of partial melting equilibria for metapelites. Journal of Metamorphic Geology 25 (5), 511–527.
URL http://onlinelibrary.wiley.com/doi/10.1111/j.1525-1314.2007.00711.x/abstract (Cited on page 43.)

Whitney, D., Seaton, N., 2010. Garnet polycrystals and the significance of clustered crystallization. Contributions to Mineralogy and Petrology 160 (4), 591–607. (Cited on page 17.)

Yamato, P., Tartèse, R., Duretz, T., May, D., 2012. Numerical modelling of magma transport in dykes. Tectonophysics 526-529, 97–109. (Cited on pages 3 and 67.)

Part V

APPENDIX

Outcrop and sampling localities and description

Point number	UTM coordinates (UTM zone 33N)		Outcrop Type	Lithology	Orientations			Samples		
	Easting (m)	*Northing (m)*			*Type*	*DipDir*	*Dip*	*Index*	*Orientation*	*Comments*
1	492893	5223251	roadcut, apparently in place large blocks, Orientations coincide with other outcrops	Micaschist, gt, ky, graphite gt 1-2cm large, densely packed few ky, graphite colours minerals	S	184	28	01	168/30	
					S	166	33	02	loose	
					L	206	16	03	loose	
					Lc2	80	17	18	loose	
					Lc2	84	24			
2	492975	5223219	outcrop, fresh surfaces due to Roatcutting,	same lithology, gt <1cm, darker more ky (see photos)	S (?)	124	25	04	132/65	
					Lm	186	18			
					S	202	37			
3	493079	5223249	loose blocks aside road					05	loose	
								06	loose	
4	493229	5223301	outcrop at switchback,	fewer gt in place, large and dense gt in blocks	S	202	37	07	147/49	good visibility of cross-cutting crenulation Cleavages Lc1 and Lc2
					S	170	30			
					S	191	27			
					Lc1	193	37			
					Lc2	257	15			
					Lc2	242	3			
5	493246	5223314	Outcrops, ca. 50m roadcut	from SW to NE: large (>10mm) densly distr. grt to small (~5mm) densly distr. grt + N-S oriented ky	S	200	36	09	172/24	largest gt of this outcrop
					Lc2	256	24	10	loose	similar to in place fine grained middle section
					S	142	30	11	242/12	mediumsized gt
					Lc1	74	5			
6	493331	5223391	loose blocks aside road	see sample descriptios				12	loose	low graphite, much gt, bright micaschist
								13	loose	amphibolite, gt, ep
								17	loose	amphibolite, weathered Exposed gt (a lot!!), ep
7	493395	5223430	outcrop					14	S 228/48 Lm 318/18	qtz layer
8	493287	5223462	outcrop					15	S 192/28 L? 168/26	small gt
9	493300	5223477	loose blocks aside road					16	loose	amphibolite, gt, ep

Outcrop and sampling localities and description

10	493257	5223269	large outcrop below switchback	same lithology, grt (1-2cm), some of them have a qtz rim	S	180	19	19	088/89
					S	211	30	20	198/21
					Lm	252	15	21	200/21
					Lc1	183	32		
11	493430	5223486	outcrop, roadcut	folded amphibolite. amp+plag+bt+-gt+-ep bt bears mineral lineation	S	202	49	22	004/66
					S	199	49		
					Lm	188	46		
					Sap (axial plane)	199	41		
					Lf (fold hinge)	194	44		
					Sap	180	50		
					Lf	192	51		
					Sap	164	56		
					Lf	190	51		
					Lf	158	53		

sample analyses overview

sample		small TS	EBSD glue	chem polished	large TS	scanned	WR analysis	SEM detailed work	EMP
03		03e	x	x		x		±	
		03f2	x	x		x			
					03f1		x		
					03i1				
					03i2				
					03j				
05					05b				
06					06b				
07		07f	x	x		x			x
		07g	x			x		±	x
		07h1	x	x		x			
		07h2	x	x		x	x	++	
		07h3	x					+	x
		07h4	x					++	x
					07i				
08		08c1	x	x		x			
		08c2	x	x		x	x		
					08b				
09					09d				
					09e				
10		10a1	x			x		++	
		10a2	x			x		++	
		10a3	x			x		+	x
		10a4	x			x	x		
		10a5	x						
		10a6	x						
		10a7	x						
		10a8	x						
11					11b				
					11c				
12					12c				
					12d				
					12i				
					12j				
15	MICA SCHIST	15c	x					++	x
					15d				
18					18a				
19					19e				
					19f				
20					20b				
13					13c				
16	AMPHIBOLITE	16b	x				x		
		16c	x						
17		17a	x				x		
		17c	x						
22		22a	x				x		

Whole rock analyses

label at GBA	GCH-2013-023-001	GCH-2013-023-002	GCH-2013-023-003	GCH-2013-023-004
label this study	03	07	08	10
[wt-%]				
SiO2	58.00	59.00	59.00	51.37
TiO2	0.73	0.73	0.80	0.79
Al2O3	23.21	23.99	23.93	28.27
FeO	8.62	6.99	7.65	8.12
MnO	0.10	0.09	0.11	0.13
MgO	1.12	0.78	0.90	0.90
CaO	1.86	0.91	0.49	2.03
Na2O	0.79	0.98	0.60	0.88
K2O	2.74	3.24	3.63	4.05
P2O5	0.13	0.09	0.10	0.12
H2O (110°C)	0.20	0.28	0.26	0.20
H3O+	< 0,1	0.94	0.78	1.44
CO2	2.16	1.65	1.30	0.81
SO3	0.02	0.02	0.02	0.02
total	99.68	99.69	99.57	99.13
[ppm]				
As	< 1	< 1	< 1	< 1
Ba	234.10	391.53	354.10	382.00
Cd	< 1	< 1	< 1	< 1
Ce	77.80	80.20	96.90	83.33
Co	< 5	10.60	10.97	10.18
Cr	116.84	120.49	129.84	140.96
Cs	< 1,5	2.95	3.25	2.45
Cu	24.25	27.40	14.77	13.24
La	32.35	41.15	36.60	41.17
Nb	22.00	25.33	24.47	23.67
Nd	25.50	45.70	< 5	< 5
Ni	19.83	17.47	12.23	19.60
Pb	22.63	33.83	30.17	45.77
Rb	105.07	124.87	132.40	177.73
Sr	176.67	191.97	172.10	232.17
V	132.60	147.77	173.60	171.27
Y	35.00	44.23	52.77	34.33
Zn	97.93	212.17	128.60	89.27
Zr	150.20	180.53	201.33	153.83
total [ppm]	1272.77	1698.19	1574.10	1620.96
total [wt-%]	0.13	0.17	0.16	0.16
total (whole sample) [wt-%]	99.81	99.86	99.73	99.29

Whole rock analyses

label at GBA	GCH-2013-023-005	GCH-2013-023-006	GCH-2013-023-007
label this study	16	17	22
[wt-%]			
SiO2	54.50	58.50	54.00
TiO2	1.25	1.50	2.55
Al2O3	14.55	12.46	13.01
FeO	10.29	11.41	10.57
MnO	0.18	0.24	0.17
MgO	6.88	4.70	4.21
CaO	9.79	9.70	9.10
Na2O	0.74	< 0,1	2.18
K2O	0.31	0.21	1.16
P2O5	0.22	0.30	0.55
H2O (110°C)	0.16	0.15	0.10
H3O+	0.87	0.54	0.29
CO2	0.08	0.08	1.84
SO3	0.01	0.01	0.03
total	99.81	99.79	99.76
[ppm]			
As	< 1	< 1	< 1
Ba	36.30	23.73	306.13
Cd	< 1	< 1	< 1
Ce	21.90	43.77	73.10
Co	26.72	16.50	44.00
Cr	235.21	167.12	97.21
Cs	< 1,5	< 1,5	< 1,5
Cu	43.52	50.54	90.11
La	8.87	19.67	32.07
Nb	12.43	13.80	50.13
Nd	< 5	36.00	< 5
Ni	121.50	50.20	74.70
Pb	16.67	22.30	8.00
Rb	7.97	4.00	23.33
Sr	363.07	252.87	421.43
V	288.23	322.67	316.00
Y	33.37	40.47	28.33
Zn	95.47	133.37	84.30
Zr	112.47	143.07	279.13
total [ppm]	1423.69	1340.06	1927.99
total [wt-%]	0.14	0.13	0.19
total (whole sample) [wt-%]	99.95	99.92	99.95

Equilibrium phase diagram for sample 07

Bulk(1)= SI(67.78)TI(0.63)AL(32.48)FE(6.72)MN(0.09)MG(1.33)CA(0.97)NA(2.17)K(4.75)O(?)H(1000) SP07 bulk

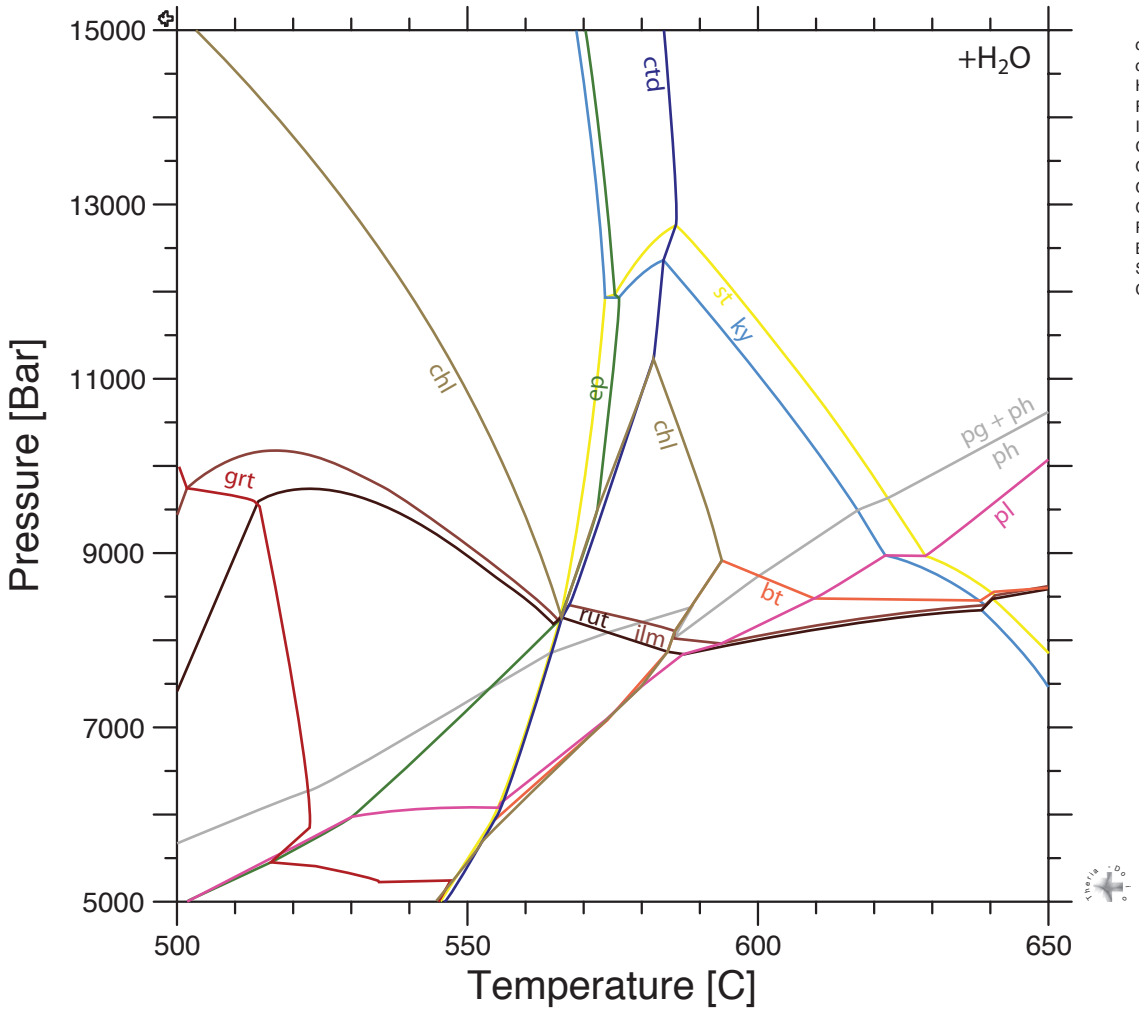

domino version: 03.01.2012
database: dbmsc
H2O: HHP98
FSP: ideal+margules
ILM: ideal
GARNET: site mixing+margules
OMPH: site mixing+margules
CHTD: ideal+margules
CHLR: site mixing+margules
PHNG: site mixing+margules
BIO: site mixing+margules
STAU: ideal+margules
CORD: site mixing

Stretch for strain localisation between garnets

sample	10a1_001			10a1_003		10a2_012
	upper left	uper right	lower right	left	right	
1mm in Illustrator	7.59	7.59	7.59	196.44	196.44	196.44
l0 in Illustaror	2.36	4.09	7.95	104.7	207.35	67.8
l in Illustrator	0.28	0.28	1.42	3.7	36.03	14.7
l0 [mm]	0.31	0.54	1.05	0.53	1.06	0.35
l [mm]	0.04	0.04	0.19	0.02	0.18	0.07
elongation **e**	-0.88	-0.93	-0.82	-0.96	-0.83	-0.78
stretch **s**	0.12	0.07	0.18	0.04	0.17	0.22

sample	10a2_015		10a4_003		10a5_006	
	left	right	left	right	left	right
1mm in Illustrator	196.44	196.44	196.44	196.44	196.44	196.44
l0 in Illustaror	149.5	104.6	92.6	77	359.1	401.6
l in Illustrator	39.8	39.8	1.54	1.54	77.1	77.1
l0 [mm]	0.76	0.53	0.47	0.39	1.83	2.04
l [mm]	0.2	0.2	0.01	0.01	0.39	0.39
elongation **e**	-0.73	-0.62	-0.98	-0.98	-0.79	-0.81
stretch **s**	0.27	0.38	0.02	0.02	0.21	0.19

sample	10a5_010		10a5_013			
	left	right	upper left	upper right	lower left	lower right
1mm in Illustrator	196.44	196.44	196.44	196.44	196.44	196.44
l0 in Illustaror	177.6	233.4	257.4	273.1	196.2	159.8
l in Illustrator	23.8	23.8	47.9	47.9	26.7	26.7
l0 [mm]	0.9	1.19	1.31	1.39	1	0.81
l [mm]	0.12	0.12	0.24	0.24	0.14	0.14
elongation **e**	-0.87	-0.9	-0.81	-0.82	-0.86	-0.83
stretch **s**	0.13	0.1	0.19	0.18	0.14	0.17

sample	10a5_15		10a6_006		10a6_012	
	left	right	left	right	left	right
1mm in Illustrator	8.72	8.72	196.44	196.44	196.44	196.44
l0 in Illustaror	2.79	3.83	157.4	136	151.8	210.3
l in Illustrator	0.44	0.44	13.5	13.5	5.7	5.7
l0 [mm]	0.32	0.44	0.8	0.69	0.77	1.07
l [mm]	0.05	0.05	0.07	0.07	0.03	0.03
elongation **e**	-0.84	-0.89	-0.91	-0.9	-0.96	-0.97
stretch **s**	0.16	0.11	0.09	0.1	0.04	0.03

sample	15c_003	
	left	right
1mm in Illustrator	196.44	196.44
l0 in Illustaror	254.4	136.2
l in Illustrator	51.8	51.8
l0 [mm]	1.3	0.69
l [mm]	0.26	0.26
elongation **e**	-0.8	-0.62
stretch **s**	0.2	0.38

COLOPHON

This document was typeset using the typographical look-and-feel `classicthesis` developed by André Miede. The style was inspired by Robert Bringhurst's seminal book on typography *"The Elements of Typographic Style"*. `classicthesis` is available for both LaTeX and LyX:

http://code.google.com/p/classicthesis/

Happy users of `classicthesis` usually send a real postcard to the author, a collection of postcards received so far is featured at:

http://postcards.miede.de/

Final Version as of June 10, 2014 (`classicthesis`).

Hagen Bender

Personal Data

Date and place of birth	14.08.1987 in Frankfurt (Oder)
Citizenship	German
Contact	Geologengasse 8 / 11 1030 Vienna, Austria +43 660 412 0 612 hagenbender@gmx.de

Education

Master of Science in Earth Sciences — June 2014
Department of Geodynamics and Sedimentology, University of Vienna
Thesis title: "Clash of Porphyroblasts: Accelerated dissolution-recipitation by mechanical interaction of porphyroblasts"

Bachelor of Sciences — October 2012
Department of Geodynamics and Sedimentology, University of Vienna
Thesis title: "Quantitative observations of structures in Rosenburg (Lower Austria)"

Undergraduate studies "Geowissenschaften" at Free University of Berlin — October 2008 - February 2010

Abitur
German secondary school graduation at Geschwister-Scholl-Gymnasium in Fürstenwalde (Spree), Germany — June 2007

Conference participation

Abstract
H. Bender, B. Huet, B. Grasemann and R. Schuster (2014): Clash of garnets - Mechanical interaction of porphyroblasts. Geophysical Research Abstracts, Vol. 16, EGU General Assembly 2014, Vienna, Austria, 27 April - 02 May 2014.

Work experience

Tutorials at the Department of Geodynamics and Sedimentology, Univerity of Vienna

Geological Mapping and Methods, Bachelor programme course — Summer Semester 2014

Quantitative Structural Geology/Tectonics, Master programme course — Winter Semester 2013

Structural Geology and Tectonics, Field trip for a bachelor programme course — Summer Semester 2013

Geological Methodology and Maps, Bachelor programme course — Summer Semester 2012

Internship
Sedimetological laboratory, Geosciences Division, Alfred-Wegener-Institute in Potsdam — August - September 2008

Miscellaneous
Work-and-travel stay in New Zealand — September 2007 - April 2008

Further qualifications and personal interersts

Language skills

English	-	fluent
German	-	mother tongue
French	-	basic knowledge

European driving licence
Classes A, B

Personal interests and hobbies
Road cycling, hiking, photography, cinema

Software skills
MATLAB

THERIAK-DOMINO

EDAX Genesis (energy-dispersive spectrometer operating software)

xT Microscope Server (*FEI Inspect S50* scanning electron microscope operating software)

SX 100 (*CAMECA SX 100* electron probe micro analyzer operationg software)

Adobe Creative Suite

Office suites (MS Office, OpenOffice.org)

References

Prof. Bernhard Grasemann, Head of Department
Department for Geodynamics and Sedimentology
University of Vienna
Althanstrasse 14/2B445
A-1090 Vienna (Austria)
+43 1 4277 53472
Bernhard.Grasemann@univie.ac.at
Relationship: Professor, supervisor (BSc and MSc) and mentor for four years

Dr. Benjamin Huet, Assistant Professor
Structural Processes Group Vienna
University of Vienna
Althanstrasse 14/2A273
A-1090 Vienna (Austria)
+43-1-4277-53311
benjamin.huet@univie.ac.at
Relationship: Professor, supervisor (MSc) and mentor for three years